PROTECT2024

9th International Colloquium on Performance, Protection & Strengthening of Structures Under Extreme Loading & Events

13 - 16 August 2024 I Singapore

CONFERENCE PROCEEDINGS

Organised by

NANYANG TECHNOLOGICAL UNIVERSITY SINGAPORE

NTU CEE Alumni Association

LIST OF TECHNICAL PAPERS

ID Number	Authors (s) – Paper Title
PS-44	***Jie Yu, Chengyi Li, Yuhang Wang , Ke Ke , Jike Tan, Ziqiang Li*** – Experimental Study On The Shear Performance Of PZ Shear Connectors In Composite Beams
PS-48	***Zhou Linren, Zheng Zewu, Shrestha Sparsh*** – Temperature Analysis Of Offshore Wind Turbine Support Tower Structure Considering The Effect Of Wind Field
PS-49	***Zhou Linren, Zheng Junbin, Zhang Haoyu –*** Finite Element Analysis For Vibration Response Of Bridge Modular Expansion Device Under Vehicle Load
PS-51	***Shuangshuang Jin, Shiyu Zhou, Jianting Zhou*** – Experimental Study On Seismic Performance Of Assembled Piers With External Corrugated Steel Plates
PS-52	***Prithvi Sangani, Kaushik Ghoshal, Anil Agarwal –*** Behavior Of Hollow Steel Tubular Columns Subjected To Low-velocity Lateral Impact By Deformable Projectile: Numerical Studies
PS-57	***Truong-Thang Nguyen, Tuan-Trung Nguyen, Thi-Nguyet-Hang Nguyen, Viet-Hung Dang, Tuan-Ninh Nguyen, Ngoc-Phuong Nguyen*** – Effects Of Concrete Spalling On Thermal-induced Compression Force In Restrained Reinforce Concrete Columns Exposed To Non-standard Fire

EXPERIMENTAL STUDY ON THE SHEAR PERFORMANCE OF PZ SHEAR CONNECTORS IN COMPOSITE BEAMS

Jie Yu[1], Chengyi Li[1], Yuhang Wang[2], Ke Ke[3], Jike Tan[3]， Ziqiang Li[1]

[1] School of Architecture and Engineering, Chongqing University of Science and Technology, Chongqing 401331, China, likoo1024@163.com.

[2] School of Civil Engineering, Chongqing University, Chongqing 400044, China, 2021047@cqu.edu.com.

[3] School of Civil Engineering, Chongqing Jiaotong University, Chongqing 400074, China.

Corresponding Author: Chengyi Li, School of Architecture and Engineering, Chongqing University of Science and Technology.

Chongqing University of Science and Technology, No. 20 Daxuecheng East Road, Shapingba District, Chongqing, China, 401331

Email: likoo1024@163.com

ABSTRACT

To investigate the influence of multiple parameters on the shear performance of (PZ shear connector) in composite beams, explore the influencing factors of the shear bearing capacity of PZ shear connectors, and provide reference for the design of steel-concrete composite structures, this paper adopts a push-out test method, with the shape of the connector opening shape and the diameter of the penetrating steel rebars as control parameters, and designs and conducts two sets of monotonic static pushout tests of six PZ shear connectors. The failure mode, shear bearing capacity, shear stiffness ductility, and load-slip curves of the PZ shear connector specimens were obtained through experiments; Emphasis was placed on the influence of the shape of the opening of the PZ shear connector under static load and the diameter of the penetrating reinforcements on the shear bearing capacity of the shear connector. The experimental results show that the PZ shear connector in composite beam has excellent shear resistance performance.

Keywords: *PZ shear connector; push-out test; failure mode; shear bearing capacity.*

1 INTRODUCTION

Shear connectors are key components that ensure that the two materials can fully play their roles in steel-concrete composite beams[1]. At present, PBL shear connectors are widely studied both domestically and internationally due to their advantages of simple manufacturing process, fast welding speed, and good stress performance[2-6]. They are widely used in civil construction and bridge engineering fields both domestically and internationally. In recent

years, with the vigorous development of prefabricated buildings by the country, scholars and engineers have also begun to innovate in the construction form of connectors, in order to better apply them to prefabricated structures and bring convenience to construction and reinforcement of damaged buildings.

When the shear connectors bear the shear force, there will be significant slippage between them and the steel beam, which is difficult to meet the requirement of controlling the slippage of the shear connectors within a small range. Nowadays, the types of PBL connectors are relatively single. Generally, the study focuses on the impact of differences in PBL shear connector size or the penetration of reinforcements on the structural shear bearing capacity. However, research on the influence of new forms and shapes of shear connectors is relatively limited. Many scholars have conducted similar studies on PBL shear connections, but there is relatively little research on further adjusting the structural form of PBL connectors. Moreover, there is still no standardized form, size, and load-bearing capacity for this type of connector, and there are no specified specimens and testing methods. There is also relatively little research and use of this type of connector.

In response to the shortcomings in the research and application of existing rigid shear connectors and prefabricated steel-concrete composite beams, this paper proposes a new type of puzzle shaped shear connector (PZ connector). Through shear connector pushout tests, the overall mechanical performance of steel-concrete composite beams is studied, and a simplified calculation method for the influence of multiple parameters on the bearing capacity of shear connectors is obtained.

2 EXPERIMENTAL PROGRAMS

2.1 Material Properties

This project launched an experiment using C40 commercial concrete material, and its mechanical properties were measured according to the "Standard Test Methods for Mechanical Properties of Ordinary Concrete" (GB/50081-2002)[7], as shown in **Table 1**. The shear performance of PZ shear connectors is closely related to the mechanical properties of the surrounding concrete. Therefore, in order to further analyse the shear performance of shear connectors, it is necessary to obtain the mechanical parameters of concrete under uniaxial stress. Due to significant differences in the size of specimens used in concrete mechanical performance tests in various national standards, this article conducts mechanical performance tests on concrete specimens of different sizes.

Table 1 Concrete performance index of push-out specimen

index / test time	f_{cu} (Mpa)	f_c (Mpa)	E_s ($\times 10^4$Gpa)
28 days	39.6	23.5	2.98
on the test	43.0	26.7	3.10

The steel beam used in this experiment is hot-rolled H-shaped steel, and the material mechanical properties of H-shaped steel and reinforcements are measured in accordance with the provisions of the "Metal Materials Tensile Test" (GB/T228.1-2010)[8]. **Figure 1** shows the geometric dimensions of the standard tensile specimens of steel plates in the section steel. The measured mechanical performance indicators of the steel in this test are shown in **Table 2**.

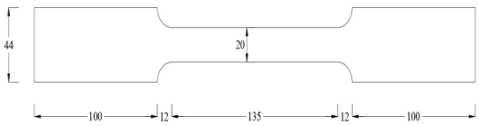

Figure 1. Detail drawing of steel tensile specimen

Table 2 Steel performance index of push-out specimen

index / test time	f_y (MPa)	f_u (MPa)	E_s ($\times 10^2$GPa)
steel	415	554	1.94
HRB400 rebar	600	750	2.0

2.2 Test Specimens

This chapter designed 3 sets of 9 push out test specimens in accordance with European Standard 4 [9](**Figure 2**, **Figure 3**). Three sets of test specimens were all PZ shear connectors in composite beams, with varying parameters including through hole shape, through reinforcement diameter, connector thickness, and the presence or absence of through reinforcements. All specimens were composed of cast-in-place concrete slabs and steel beams, as shown in Figure. 4, the elevation view, side view, plan view, and the relationship diagram between the steel beam and PZ shear connector of the test specimen are presented. The processing of shear connectors is mainly completed in the factory, cutting and welding small steel plates to meet the dimensions required by the drawings. H-shaped steel is welded from a 14mm flange plate and a 9mm web plate. The same batch of specimens has multiple sizes, and the required number of connectors is determined based on the number and shape of through holes. In this study on the shear performance of PZ shear connectors in steel-concrete composite beams, experimental specimens were launched. Considering the size of PZ connectors as 320 × 140 × (8) 10mm, the detailed size diagram of PZ connectors is shown in **Figure 4**. The cross-sectional size of H-shaped steel is HW340 × 250 × 9 × 14mm, with a length of 600mm, and the steel is Q345b; The cross-sectional size of the concrete slab is 600 × 500 × 160mm, and the thickness of the concrete protective layer is 20mm. The detailed parameters of the specimen are shown in **Table 3.**

Table 3 The parameter of push-out test of PZ connector

Specimens	Steel (mm)	Concrete (mm)	Hole	d_{st} (mm)	d (mm)	t (mm)
P-C-12-40-10	340×250×9×14	600×500×160	circular	12	40	10
P-E-12-40-10	340×250×9×14	600×500×160	elliptic	12	40	10
P-C-16-40-10	340×250×9×14	600×500×160	circular	16	40	10

Note: Naming method: the first letter P refers to the specimen; The second letter C represents an elliptical hole, and E represents an elliptical hole; The third digit d_{st} represents the diameter of the reinforcement t, which is 12mm and 16mm respectively; The fourth digit d refers to the opening diameter of the PZ connector, which is 30mm and 40mm respectively; The fifth digit t represents the thickness of the PZ connector, which is 8mm and 10mm respectively.

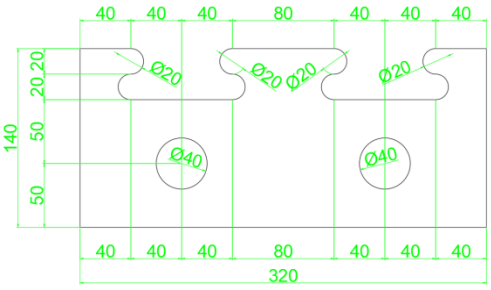

Figure 2. PZ shear connector size (circular hole)

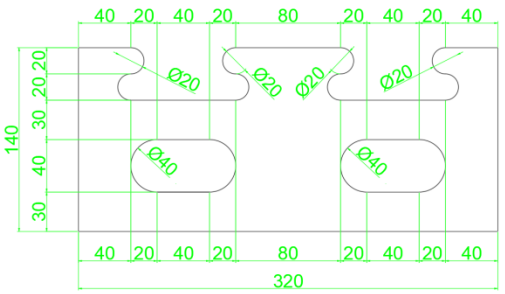

Figure 3. PZ shear connector size (elliptic hole)

2.3 Test Setup

A 200t hydraulic jack was used for loading, and the electro-hydraulic servo actuator is controlled through a software control system of the push-out tests. Force control or displacement control can be selected to achieve real-time control of loading. The load is measured in real-time using a 200t tension and compression force sensor, and the DHDAS dynamic signal acquisition and analysis system collects stress-strain data in time. The relative slip value between the steel beam and concrete of the specimen was measured in real-time by connecting four YHD-100 displacement meters with a 90° angled L-shaped aluminum sheet before and after the specimen, as shown in **Figure 5.**

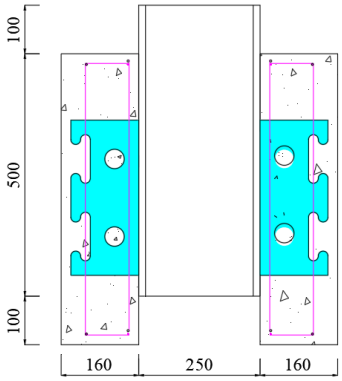

(a) elevation of PZ shear connector push-out specimen

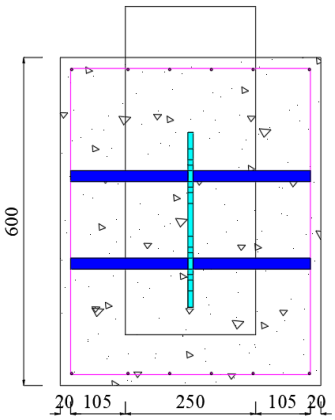

(b) side view of PZ shear connector push-out specimen

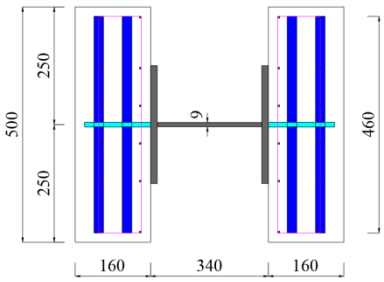

(c) plan view of PZ shear connector push-out specimen

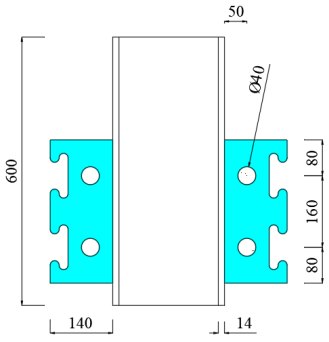

(d) relationship between the steel beam and PZ connector

Figure 4. Steel concrete composite beam PZ shear connector specimens

All 3 groups of specimens were subjected to a monotonic graded loading system: pre loading was carried out at a rate of 30% of the bearing capacity (**Figure 6**.), with a graded loading rate of 100kN/min; 80% of the calculated bearing capacity is the yield load, which is preloaded to the yield load stage and subjected to graded loading at a rate of 50kN/min. The displacement corresponding to reaching the yield load is defined as the yield displacement $\triangle y$; After reaching the yield load, load in increments of $\triangle y$, and slowly load when approaching the expected calculated bearing capacity; After reaching the peak, continue to load at a certain rate until the load starts to decrease until it finally drops to zero. Stop loading and the test ends.

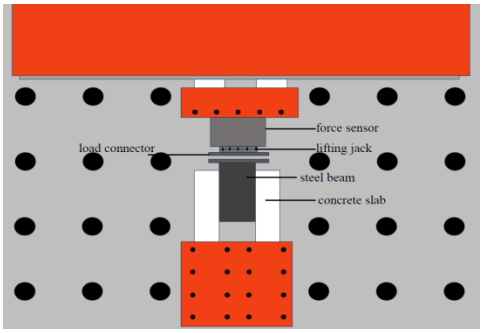

(a) push-out loading equipment

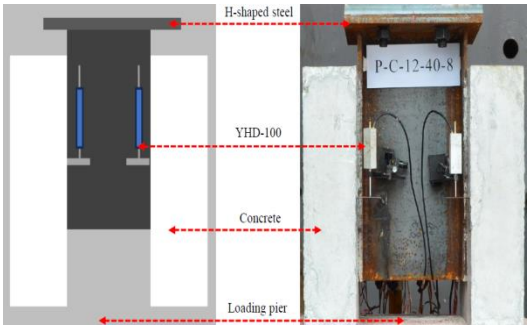

(b) measuring device of push-out test

Figure 5. loading equipment and measuring device of push-put test

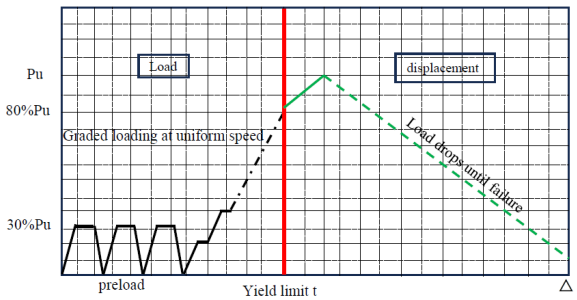

Figure 6. Loading system of push-out test

3 RESULTS AND DISCUSSION

3.1 Analysis of Failure Modes

Figure 7 shows a photo of a typical failure mode during the push out test of PZ shear connectors. In the initial stage of monotonic loading, the interface slip of the specimen increases linearly with the load. From the appearance of the specimen, there is no obvious failure phenomenon between the concrete slab and the steel beam; As the load gradually increases, the stiffness of the specimen decreases significantly. As the load increases, vertical cracks, horizontal cracks, diagonal cracks, zigzag cracks, and circumferential cracks gradually appear, extend and widen, and develop towards the surrounding areas; Entering the elastic-plastic stage, some specimens generate small microcracks around the outer surface of the concrete during this stage; When approaching the peak load, the sound of concrete crushing can be heard, and cracks on the outer surface of the concrete slab gradually penetrate, forming more obvious horizontal cracks and 45° diagonal cracks; After the load reaches its peak, the interface slip continues to increase while the load decreases; When the load drops to around 85% of the peak value, there is a significant separation between the steel beam and the concrete slab, which widens as the load increases. There are continuous obvious cracks on the inner and outer surfaces of the concrete

slab, and the concrete slab is locally crushed. Due to the lateral reinforcement effect, the concrete slab does not break, and concrete cracks and falls off significantly when it is damaged.

From the experimental phenomena of the specimens pushed out from **Table 4**, it can be concluded that the main failure modes of the PZ shear connector are concrete cracking or even prying failure in the groove of the PZ shear connector, local crushing of the concrete, as well as the appearance of eight through cracks and vertical cracks. The severely damaged specimens have a large area of concrete lifting and falling off, and even the internal connection structure can be seen, as well as significant separation between the steel beam and the concrete. The comparison of failure modes between two sets of specimens is shown in **Figure 8**, **Figure 9**.

(a) Phenomenon of concrete failure in PZ shear connectors pushed out of specimens

(b) The failure modes of the separation of steel beams and concrete and PZ shear connector

Figure 7. The phenomenon of push-out of PZ connector push-out specimens

Table 4. Summary of the test phenomenon of PZ shear connector push-out specimens

Specimens	Phenomenon of push-out specimens	
	Bearing capacity (kN)	Failure modes of phenomenon
P-C-12-40-10-1	968	When loaded to 800kN, 45 ° cracks appeared on both sides of the concrete slab, and the concrete continued to crack, gradually deepening the cracks.
P-C-12-40-10-2	1153	When loaded to 900kN, a loud noise occurred, and the diagonal cracks penetrated to the bottom.
P-C-12-40-10-3	1140	Internal damage accompanied by loud noises, gaps between steel beams and concrete, and extensive lifting of concrete.
P-C-16-40-10-1	1720	When loaded to around 1370 kN, a large area of concrete falls and multiple diagonal 45 ° cracks and vertical cracks are added.
P-C-16-40-10-2	1613	Concrete crushing, separation between steel beams and concrete, multiple cracks appearing at the contact between steel beams and concrete before failure.
P-C-16-40-10-3	1580	Load to 1200 kN, concrete severely pried up.
P-E-12-40-10-1	1125	When loaded to $3\triangle y$, the concrete is pried up.
P-E-12-40-10-2	1043	The gap between the steel beam and concrete creates transverse cracks, which continue to increase by about 5mm, and the concrete cracks and falls off.
P-E-12-40-10-3	1230	When loaded to 900 kN, the cracks gradually develop and extend, appearing as claw shaped cracks that continue to widen and develop in all directions.

（a）P-E-12-40-10 before destruction

（b）P-C-12-40-10 before destruction

（c）P-E-12-40-10 in failure stage

（d）P-C-12-40-10 in failure stage

（e）P-E-12-40-10 separation of steel beams and concrete

（f）P-C-12-40-10 separation of steel beams and concrete

Figure 8. The difference of failure modes between specimen P-E-12-40-10 and P-C-12-40-10

（a）P-C-16-40-10 before destruction

（b）P-C-12-40-10 before destruction

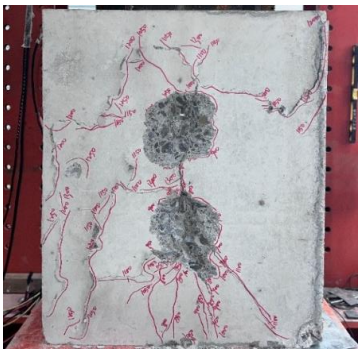

（c）P-C-16-40-10 in failure stage

（d）P-C-12-40-10 in failure stage

（e）P-C-16-40-10 separation of steel beams and concrete

（f）P-C-12-40-10 separation of steel beams and concrete

Figure 9. The difference of failure modes between specimen P-C-16-40-10 and P-C-12-40-10

3.2 Load-Displacement Relationships

The average longitudinal shear force value (F) of the two interfaces of the test piece is obtained by dividing the load value collected by the force sensor of the reaction frame jack by 2; The average longitudinal interface slip value (s) of the specimen is calculated by averaging the interface slip values of four measuring points collected by four YDH-100 displacement meters. Thus, the interface load (F) - slip (s) relationship curves of the PZ shear connector specimens were obtained. **Figure 10** shows the interface load F-s relationship curves.

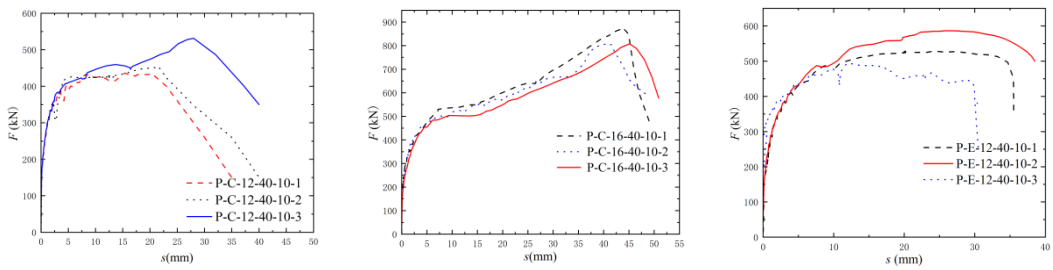

(a) P-C-12-40-10 (b) P-C-16-40-10 (c) P-E-12-40-10

Figure 10. The F-s relation curves of push-out of PZ connector

From the above curves, it can be seen that the load slip curves of all the specimens can be described as follows: (a) in the elastic stage, the concrete tenon and the penetrating reinforcement jointly provide shear resistance, and the load and slip increase linearly; (b) After the elastic stage, it enters the yield stage, and the concrete tenon fails. The reinforcements penetrate and bear the main load, and slip rapidly develops with a slight increase in load; (c) After the reinforcements yield, they enter the strengthening stage, and the load increases rapidly with the slow development of slip; (d) After the steel reinforcement is damaged, it enters the failure stage, and the load significantly decreases as the sliding increases.

3.3 Effect of shape of the opening of the PZ shear connector

According to Table 4, the average peak bearing capacity of specimen P-E-12-40-10 pushed out by PZ shear connector (elliptical through hole) has increased by 4.6% compared to specimen P-C-12-40-10 pushed out by PZ shear connector (circular through hole). This is mainly due to the fact that the through hole area of PZ shear connector is 10048mm^2, which is 200% higher than that of P-C-12-40-10, and the increase in shear bearing capacity is relatively low, the difference between the two results in a double difference in the shear force borne by the concrete tenon.

The PZ shear connector (elliptical hole) pushes out specimen P-E-12-40-10. During static load loading, cracks mainly concentrate at 3/5 of the middle and upper parts, and the load reaches around the yield load. Concrete cracks accompanied by brittle sound and more circumferential cracks are generated. During displacement loading, concrete cracking mainly occurs around the concrete slab and is lifted, with steel beams separating earlier (about 3mm).

3.4 Effect of the diameter of the penetrating reinforcements

As shown in Table 4, the average peak bearing capacity of specimens P-C-16-40-10 pushed out of PZ shear connectors (with a diameter of 16mm through reinforcements) has increased by 33.8% compared to specimens P-C-12-40-10 pushed out of PZ shear connectors (with a diameter of 12mm through reinforcements). The main difference lies in the cross-sectional area of the reinforcements. The cross-sectional area of the reinforcements pushed out of specimens P-C-16-40-10 is 1608mm^2, while the cross-sectional area of the reinforcements pushed out of specimens P-C-12-40-10 is 904 mm^2, with a difference of 43.7%, The difference in average peak bearing capacity is mainly caused by the difference in the portion of shear force borne by the penetrating reinforcements.

The PZ shear connector (with a reinforcement diameter of 16mm) is used to push out specimens P-C-16-40-10. During static load loading, when the load is loaded to 800kN, more cracks appear on both sides of the concrete. As the load increases, the cracks continue to develop and there is a trend of circumferential cracks appearing. When the load reaches around 900kN, circumferential cracks are obvious, and vertical, oblique, and transverse cracks continue to increase, causing a large area of concrete to crack and fall off.

CONCLUSIONS

In this study, this article focuses on the pushout test research of PZ shear connectors in steel-concrete composite beams under static load. Further parameterization analysis of the shear bearing capacity of PZ shear connectors was conducted, combined with experimental phenomena, results, and shear resistance mechanism of PZ shear connectors. The following conclusions were drawn:

(1) The shape of the through hole of the PZ shear connector results in different parts of the concrete tenon resisting the shear flow at the interface. The PZ shear connector with elliptical holes has a higher interface shear bearing capacity when pushed out of the specimen;

(2) As the diameter of the reinforcement through the PZ shear connector increases, the part of the reinforcement that bears the shear flow increases when the entire specimen resists

longitudinal shear, and the shear resistance of the cross-section of the specimen is significantly enhanced.

ACKNOWLEDGMENTS

The authors gratefully acknowledge the support provided by National Natural Science Found ation of China (No. 52108117), Chongqing Natural Science Foundation (No. CSTB2022NSCQ-MSX1242), Special Funding of Chongqing Postdoctoral Research Programs (No. 2021XM3045), Chongqing Construction Science and Technology Plan Project: Chengkezi 2023 No.1-1.

REFERENCES

[1] Shariati, A. (2012). Various types of shear connectors in composite structures: a review. Int.J. Phys. Sci. 7(22), 2876–2890.

[2] Kim, S.H. (2016). Y-type perfobond rib shear connectors subjected to fatigue loading on highway bridges. J. Constr. Steel Res. 122, 445–454.

[3] Kim, S.H. (2015). Shear resistance characteristic and ductility of Y-type perfobond rib shear connector. Steel Compos. Struct. 18(2), 497–517.

[4] Chu, T.H.V. (2016). Resistance behaviors of a newly puzzle shape of crestbond rib shear connector: an experimental study. Steel Compos. Struct. 21(5), 1157–1182.

[5] Yang Y, Chen Y. (2018). Experimental study on mechanical behavior of PBL shear connectors. Journal of Bridge Engineering, 23(9): 04018062.

[6] Yang T, Liu S, Qin B. (2020). Experimental study on multi-bolt shear connectors of prefabricated steel-concrete composite beams. Journal of Constructional Steel Research, 173: 106260.

[7] National Standards of the People's Republic of China GB50010-2010 Code for Design of Concrete Structures. (2010). China Construction Industry Press.

[8] Industry standards of the People's Republic of China GB/T228.1-2010 Metallic Materials Tensile Testing-Part I: Room Temperature Test Method Beijing. (2010). China Construction Industry Press.

[9] BS EN1994-1-1. Eurocode 4: Design of composite steel and concrete structures: Part 1.1: General rules and rules for building. (2004). London: British Standards Institution.

TEMPERATURE ANALYSIS OF OFFSHORE WIND TURBINE SUPPORT TOWER STRUCTURE CONSIDERING THE EFFECT OF WIND FIELD

Zhou Linren[1]*, Zheng Zewu*[2]*, Shrestha Sparsh*[3]

[1] Associate Professor, School of Civil Engineering and Transportation, South China University of Technology, zhoulinren@scut.edu.cn.

[2] Postgraduate, School of Civil Engineering and Transportation, South China University of Technology, 1845102031@qq.com.

[3] Undergraduate, School of Civil Engineering and Transportation, South China University of Technology, sparsh_crestha@hotmail.com.

Corresponding Author: Zhou Linren, PhD, A.P.

Guangzhou, Guangdong, China, 510640

Email: zhoulinren@scut.edu.cn

ABSTRACT

Temperature is an important load on offshore wind turbine support structures, and environmental wind is the major factor affecting the structure's temperature. This study focuses on offshore wind turbine support structures in oceanic wind environments. Specifically, it investigates the support tower, which experiences the most prominent temperature effects. Considering the influence of wind field local characteristic, a finite element (FE) calculation method for the structural temperature field is proposed. Initially, a FE transient analysis model of the temperature field for the wind turbine tower structure is established. Subsequently, the surface wind field of the wind turbine support tower structure in the marine environment is simulated and analysed to obtain wind speeds at various points on the tower surface under different incoming wind speeds. Following this, Type III thermal boundary conditions for heat exchange between the tower surface and the external environment are established based on local wind speeds. The FE transient thermal analysis method is then applied to calculate the temperature field of the wind turbine support tower structure. Finally, the temporal and spatial characteristics of the temperature field under different wind speeds are analysed and discussed through comparative analysis. By considering the local characteristics of the structural wind field, consistent with actual engineering situations, the time-varying temperature field of the structure can be calculated more accurately, which provides a key theoretical basis and technical support for the design of offshore wind turbine support structures, service state identification, and safety management.

Keywords: *Offshore Wind Power, Support Tower Structure, Temperature Field, Finite Element Analysis, Localized Wind Characteristics.*

INTRODUCTION

Wind energy, as a clean and environmentally friendly renewable energy source, has been rapidly developed and widely used in various countries. Over the past decade, global installed wind power capacity has grown considerably, with onshore wind products reaching power ratings of up to 7 MW and offshore wind products reaching 16 MW. In offshore wind power construction, the design of the support structure is an essential part of the whole offshore wind turbine design. Therefore, the bearing performance requirements for wind turbine support structures are more stringent. The harsh marine environment, characterized by high temperatures, intense radiation, and the slender and towering metal structure system, makes the temperature effect on offshore wind turbine support structures substantial, complex, and variable. However, in the design, operation, and maintenance of wind turbine support structures, temperature loads have not received adequate attention and are often overlooked.

In recent years, research scholars have achieved fruitful results in the calculation and analysis of the structural temperature field[1]. In terms of building structure, Zhang et al.[2] conducted structural temperature field monitoring and proposed a set of concrete temperature field calculation methods based on the ultra-long concrete project of the new Xiamen North Railway Station. Wang Jintao et al.[3] simulated the transient temperature field of a large-span diagonal-legged steel tube truss structure and verified that the temperature effect on the structure is not negligible. Concerning bridge structures, Zhu et al.[4] proposed a new method to simulate the non-uniform temperature field of truss suspension bridges under solar radiation. Regarding offshore wind turbine structures, Ye et al.[5] verified the degree of influence of temperature loading on the safety of jacket-type offshore wind turbine support structures. Current research progress in computational analysis of structural temperature fields mainly focuses on housing structures[6] and bridge structures[7-9]. However, there are fewer studies on the temperature field simulation of wind turbine supported tower structures, despite the considerable impact of temperature loading on these structures during service. Therefore, it is necessary to calculate and analyze the temperature field of wind turbine supported tower structures.

One of the key factors affecting the accuracy of structural temperature field simulations is the convective heat transfer coefficient of the surface. The magnitude of the convective heat transfer coefficient significantly depends on the wind speed on the surface of the structure. Most structures are thermally analyzed without considering wind effects, assuming a constant wind velocity across all points on the surface. However, wind speeds vary across the structure's outer surface, considerably impacting the convective heat transfer coefficient and consequently affecting the accuracy of the thermal analysis results. Xu et al.[10] considered the actual wind field distribution around a streamlined steel box girder, revealing substantial wind influence on temperature distribution results. Despite abundant offshore wind resources,

research has mainly focused on the wind field's effect on the efficiency of wind power generation and wind-resistant design for wind turbine blades and support structures. However, there are no reports on the research considering temperature loads and the effects of wind fields on support structures in offshore wind turbine systems.

In this paper, finite element (FE) analysis and research are conducted to consider the effect of the wind field on the supporting tower structure with the most considerable temperature effect. Firstly, the FE transient analysis model of the temperature field of the wind turbine tower structure is established. Secondly, the wind field around the cylindrical structure of the tower is simulated. Considering the local characteristics of the wind, the wind speed at each point on the surface of the turbine tower structure is calculated under different incoming wind speeds. Finally, the convective heat transfer coefficients and Type III thermal boundary conditions on the surface of the tower structure are calculated based on the refined wind speed. A transient thermal analysis method is then used to calculate the temperature field of the offshore wind turbine support tower structure. The effects of different wind fields on the temperature of the tower structure are comparatively analyzed to determine its service temperature loading pattern, which provides an important theoretical basis and technical support for the design of offshore wind turbine support structures, service state identification, and safety management.

SUPPORT STRUCTURE OF OFFSHORE WIND TURBINE

The offshore wind turbine support structure studied in this paper is a large offshore steel structure located in the offshore area of southern China. It comprises a pipe pile foundation, a jacket, a transition section (including flange, platform diagonal bracing, platform, etc.), and a tower. The total height of the support structure is 146.5m, with the pipe pile foundation standing at 37.5m, the jacket at 17.8m, the platform at 0.2m, and the tower tube at 91m, as illustrated in Figure 1. The material used to make this support structure is mainly Q345 steel, and the four leading tubes are connected to their corresponding pile foundations by sleeve grouting. Due to the requirements of actual engineering construction, the entire tower is composed of 5 sections of variable cross-section steel cylinders connected by ring flanges, with the largest diameter at the bottom of the tower being 6.5m and the smallest diameter at the top being 4.0m. The thickness of the tower also decreases with the increase in height, and the average thickness of the entire tower is 36mm.

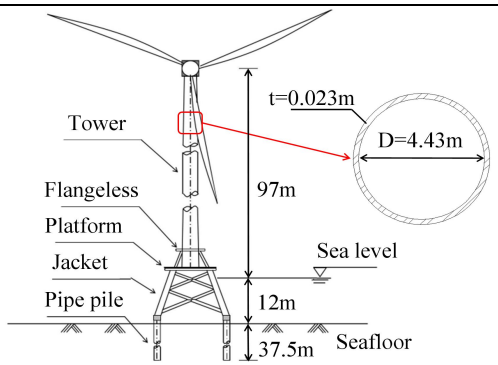

Figure 1. Sketch of wind turbine structure

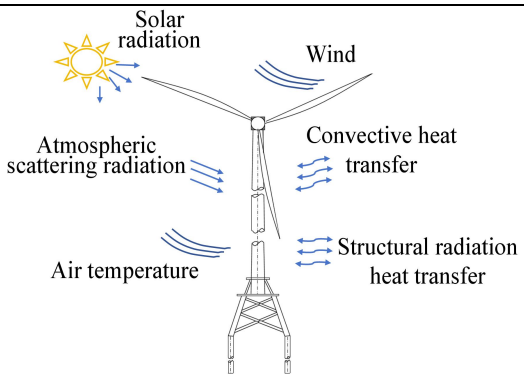

Figure 2. Thermal environments

FE MODEL FOR THERMAL ANALYSIS

Heat exchange processes between structure and the environments

Theory of convective heat transfer

Thermal convection is the phenomenon of heat exchange between a solid surface and the fluid it contacts due to a temperature difference. The convective heat transfer coefficient on the surface of the wind turbine tower structure characterizes the heat transfer capacity between the structure's surface and the surrounding air. It is defined as the amount of heat exchanged per second per square meter of area when the temperature difference is 1°C, with units of W/(m^2·K). Thermal convection can be calculated using Newton's cooling equation:

$$q_c = h_c(T_s - T_a) \tag{1}$$

Numerous studies have shown that the convective heat transfer coefficient on the surface of a structure is mainly related to the wind speed[11-15]. Therefore, finely analyzing the wind field distribution around the columns and obtaining more accurate convective heat transfer coefficients on the surface of the structure is essential for accurately simulating the temperature field of the tower structure. This paper uses the convective heat transfer coefficient calculation method proposed by Guan[16]. The formula is as follows:

$$h_c = 6.31 \times W_s^{0.656} + 3.25 \times e^{-1.91 W_s} \tag{2}$$

In the equation, q_c represents the thermal convective heat flow density; h_c is the convective heat transfer coefficient; T_s is the surface temperature of the object; T_a is the temperature of the surrounding fluid, which can be considered as the ambient air temperature; and W_s is the wind speed.

Theory of radiation heat transfer[17]-[19]

Thermal radiation is the process through which an object absorbs and emits radiation. For thermal radiation between two or more different objects, each emitting and absorbing radiation simultaneously, the energy transfer between them can be calculated using the following equation:

$$q_r = \varepsilon C_s A_1 F_{12} (T_1^4 - T_2^4) \tag{3}$$

In the equation, ε represents the material emissivity; C_s is the radiation coefficient of the blackbody with a value of $55.67\times10^{-8} W/(m^2\cdot K^4)$; A_1 is the area of radiating surface 1; F_{12} is the shape coefficient from radiating surface 1 to radiating surface 2; and T_i is the absolute temperature of radiating surface i, in K.

The radiation environment in which the wind turbine support structure is exposed in the service environment is shown in Figure 2, including direct solar radiation, scattered radiation, thermal radiation from the structure itself, etc. The calculation method of each radiation and thermal boundary is referred to in reference[20].

FE thermal analysis model of the tower cross section

The tower cross-section is divided into two parts: an outer section of steel ring and an inner section of air. The outer diameter of the ring is about 4.48m, the inner diameter is 4.43m, and the thickness is 23mm, as shown in Figure 3. When establishing the FE thermal analysis model of the tower cross-section, the material properties of each element need to be defined according to the actual situation. Specific element material properties are listed in Table 1. The FE modeling of the steel and air sections was performed using the PLANE55 2D thermal analysis element. Additionally, to consider the influence of heat radiation between the inner surfaces of the tower, the inner surface is attached to a two-dimensional heat transfer rod element LINK32 with two degrees of freedom of temperature (Heat transfer is possible between nodes). The radiation matrix cell option was defined with the AUX12 command, and the radiation matrix was modeled with the supercell MARIX50. These methods were used to calculate the temperature field distribution of the tower structure throughout the day.

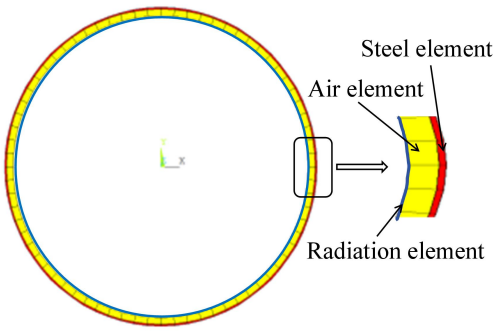

Figure 3. FE model of tower considering radial elements

Table 1. Element material properties

Parameter	Internal Air	Steel
Modulus of elasticity (*Pa*)	2.00×10^{-10}	2.09×10^{11}
Poisson's ratio	0.00	0.30
Density (kg/m^3)	1.20	7850.00
Coefficient of linear thermal expansion 1/°C	1.20×10^{-5}	1.20×10^{-5}
Thermal conductivity *W/ (m·K)*	0.026	60.00
Specific heat capacity *J/(kg·K)*	1.01	508.00
Emissivity ε	0.00	0.75
Absorption rate v	0.00	0.65

SIMULATION OF LOCAL WIND FIELD

Numerical simulation of the cylindrical winding of a two-dimensional tower cross-section is conducted using the Fluent analysis module of ANSYS software. The cylinder has a diameter of 4.47m, and the incoming wind speed is 10 m/s. The air density is 1.225 kg/m^3, and the coefficient of viscosity of air motion is 1.5×10^{-5} m^2/s at room temperature. Following model size setting, boundary region setting, mesh delineation, fluid calculation, and related steps, the wind field simulation calculation model of the tower cylindrical winding is obtained (Figure 4). The fluid flows from left to right, with the left side set as the velocity inlet and the right side as the free outflow. The upper and lower boundaries are no-slip solid-wall boundaries. The computational area of the rectangle is 40D×20D (D is the diameter of the cylinder), with the modeled upstream incoming slip area at 10D and the downstream wake area at 30D. The cylinders are each 10D from the upper and lower boundaries. The wind field calculation results for an incoming wind speed of 10 m/s are illustrated in Figure 5. The wind speed varies noticeably across the surface of the cylinder, with differences between the maximum and minimum wind speeds of up to 18.6 m/s.

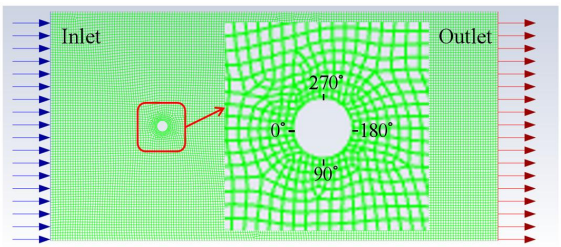

Figure 4. FE model for wind field calculation

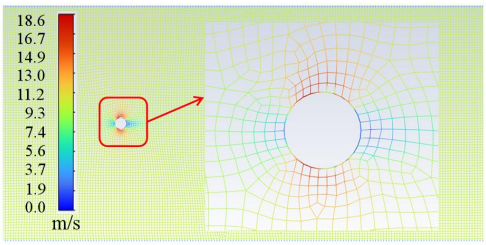

Figure 5. Wind speed field

STRUCTURAL TEMPERATURE FIELD CALCULATION

Structural temperature field considering the influence of wind field

The typical sunny weather data for July 25, 2022, are selected to study the daily temperature variation characteristics of the tower. The incoming wind with a wind speed of 10 m/s is set, and the radiation amount at each point is controlled to be the same. Based on the two working conditions of not considering the influence of the wind field and considering the influence of the wind field, the temperature field distribution of the structure throughout the day is calculated using transient heat at 3-hour intervals. When considering the influence of the wind field, the temperature field distribution remains consistent under different incoming wind speeds. Figure 6 illustrates the temperature field of the tower cross-section with an incoming wind speed of 10 m/s. When not considering the influence of the wind field, heat radiation and convection are equal at all points on the structure's surface at any given moment, resulting in uniform temperatures across the structure. When not considering the influence of the wind field, heat radiation and convection are equal at all points on the structure's surface at any given moment, resulting in uniform temperatures across the structure. The average temperatures of the structure throughout the day were essentially the same regardless of whether the wind field's effect was considered or not, with the largest difference being approximately 0.38°C at the moment of highest structure temperature. Considering the wind field characteristics, the maximum temperature difference of the structural cross-section during the daytime moments exceeds 2°C, with the maximum temperature difference reaching 7.02°C as shown in figure 7. Because considering the wind field effects around the tower leads to considerable variation in convective heat transfer coefficients at each point on the structure's surface, causing substantial temperature discrepancies across the cross-section. Therefore, it is necessary to consider wind field effects when simulating the temperature field of a tower structure.

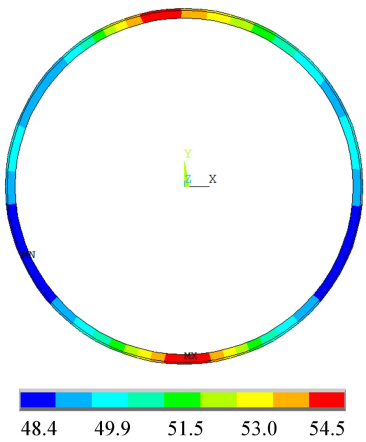

Figure 6. Temperature field (13:30)

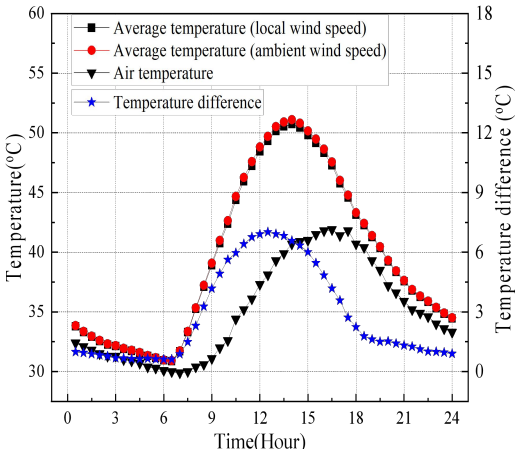

Figure 7. Average & Maximum temperature difference

Effects of wind field characteristics on structural temperature

(1) Distribution of wind field around the column at different wind speeds

Figure 8 displays the wind field distribution around the tower structure for different incoming wind speeds. As the incoming wind speed increases, the wind speed at each point on the structure's surface also increases, with minimized speeds on the windward and leeward sides. Notably, large wind speed distributions occur around wind angles of attack of 70° and 120°. Six angular position points at 0°, 30°, 60°, 70°, 120°, and 180° are selected on the surface of the circular tower cylinder. The ratio of actual wind speed to incoming wind speed at these points is extracted and calculated, as shown in Figure 9. The wind speed is consistently lower at the windward and leeward positions compared to the incoming wind speed. The surface wind speed is most amplified around 60°-70° compared to the incoming wind speed. The amplification coefficient of the local wind speed on the incoming wind speed at the same location point varies less with increasing wind speed. This analysis highlights the significant difference between the wind speed on the tower's surface and the incoming wind speed, emphasizing the importance of considering local wind speed at each surface point for calculating thermal boundary conditions in determining a more reasonable and accurate temperature field.

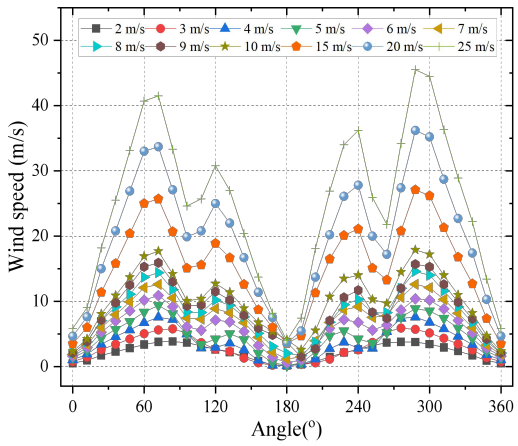

Figure 8. Surface wind speed

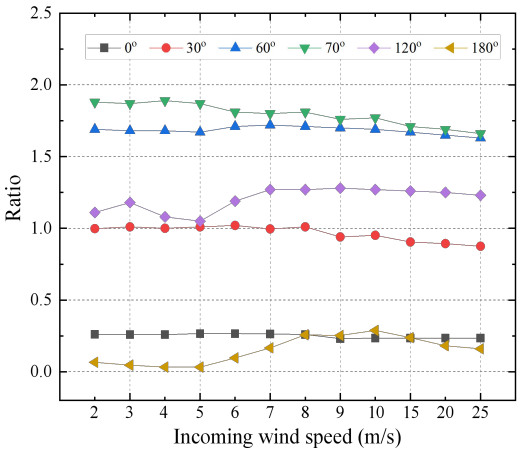

Figure 9. Surface relative wind speed

(2) Distribution of wind field around the column at different wind speeds

Simulation of the structural wind field and calculation of the structural temperature field are carried out for eleven different wind speeds ranging from 2 m/s to 25 m/s. The results of the calculation of the maximum temperature difference and the average temperature difference are presented in Figure 10 and Figure 11, respectively. Figure 10 illustrates that the maximum temperature difference when analyzing the structure's temperature field considering wind field characteristics at low, medium, and high wind speeds all exceeds 6.5°C during the

daytime.Furthermore, at wind speeds below 5 m/s, the maximum temperature difference of the tower structure cross-section increases with increasing wind speed, whereas it decreases with increasing wind speed above 5 m/s. In the wind speed range of 3 m/s to 7 m/s, the maximum temperature difference between the temperature field calculated for the structure considering wind field characteristics and without considering them is largest, exceeding 9°C. Figure 11 indicates minimal difference in the overall average temperature of the tower structure between considering and not considering wind field characteristics, both within the range of 2°C. This suggests that wind field distribution has little impact on the overall average temperature of the tower structure, mainly because it has minimal effect on the average wind speed and convective heat transfer coefficient at each point of the structure.

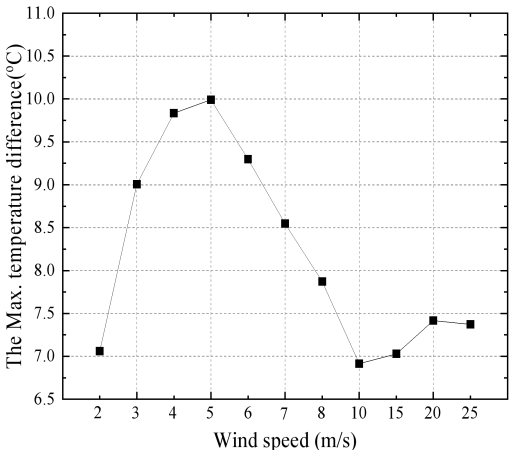

Figure 10. The Max. temperature difference

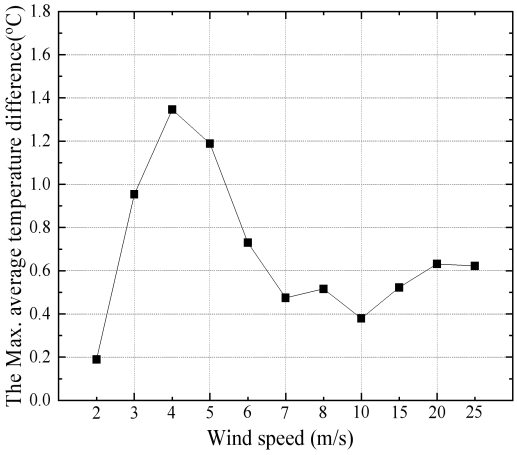

Figure 11. Average temperature difference

CONCLUSION

Considering the influence of local wind characteristics on the surface of the structure, a FE analysis method of the temperature field of the offshore wind turbine support tower structure is carried out, and the following main conclusions are obtained:

(1) Under constant incoming wind speed, the surface wind speed of the tower structure is the smallest on the windward and leeward sides and is the largest at an angle of about 60°-70°. As the incoming wind speed increases, the difference between the maximum and minimum wind speeds on the surface of the tower structure increases, and the ratio of the surface wind speed to the incoming wind speed at the same point remains relatively constant.

(2) Under the two conditions of considering the wind field characteristics (local wind speed at each point) and not considering them (ambient incoming wind speed), the overall average temperature of the tower structure at each time in a day does not differ much, with the difference within the range of 0.38°C.

(3) Considering the local characteristics of the wind field, the temperature difference within the tower section increases with the increase of the overall temperature of the structure, particularly during daytime hours. In the wind speed range of 0 m/s - 25 m/s, the maximum temperature difference of the cross-section initially increases and then decreases with the increase in wind speed. In particular, the temperature difference in the range of incoming wind speed of 3 m/s - 7 m/s is substantial, with a maximum of up to 10°C.

ACKNOWLEDGMENTS

This work is supported by the International Science & Technology Cooperation Program of Guangdong Province (2023A0505050155), the National Natural Science Foundation of China (52078220) and the International and Hong Kong, Macao and Taiwan Talents Communication Program of Guangdong Province.

REFERENCES

[1] Li, L., & Shan, Y., & Jing, Q. (2023). Global temperature behavior monitoring and analysis of a three-tower cable-stayed bridge. *Engineering Structures*, 295: 116855.

[2] Zhang, H S., & Bu, F M., & Nie, J G. (2024). Temperature simulation and thermal effect research on extremely long-span concrete frame structure. *Engineering mechanics*, 1-9.

[3] Wang, J T., & Liu, Y F., & Fan, J S. (2023). Analysis on non-uniform temperature field of large-span steel truss structure with inclined leg. *Engineering mechanics*, 41(01): 208-218.

[4] Zhu, Y., & Sun, D., & Guo, H. (2023). Fine analysis for non-uniform temperature field and effect of railway truss suspension bridge under solar radiation. *Journal of Constructional Steel Research*, 210: 108098.

[5] Ye, W X. (2021). Finite element model updating and safety assessment of jacket-type offshore wind turbine support structures. South China University of Technology.

[6] Zhou, M., & Fan, J S., & Liu, Y F. (2020). Analysis on non-uniform temperature field of steel grids of beijing daxing international airport terminal building core area considering solar radiation. *Engineering Structures*, 37(05): 46-54+73.

[7] Wang, J T., & Liu, Y F., & Zhou, M. (2023). Deformation prediction of large-span spatial structure considering adverse weather conditions. Structures. *Elsevier*, 50: 508-523.

[8] Wang, A., & Zhang, Z., & Lei, X. (2021). All-Weather thermal simulation methods for concrete maglev bridge based on structural and meteorological monitoring data. *Sensors*, 21(17): 5789.

[9] Fu, M., & Liang, Y., & Wu B. (2022). Research on Deformation Analysis and Rehabilitation for a Beam–Arch Combination Bridge Suffering an Extreme Temperature Field. *Applied Sciences*, 12(14): 6909.

[10] Huang, X., & Zhu, J. (2021). Temperature analysis of steel box girder considering actual wind field. Engineering Structures, 246: 113020.

[11] Guo, L., & Zhong, L. (2011). Thermal conductivity and heat transfer coefficient of concrete. *Journal of Wuhan University of Technology-Mater. Sci. Ed.*, 26(4): 791-796.

[12] Riding, K A., & Poole, J L., & Schindler A K. (2011). Temperature boundary condition models for concrete bridge members. *ACI Materials Journal*, 2007, 104(4): 379-387.

[13] Larsson, O., & Thelandersson, S. (2011). Estimating extreme values of thermal gradients in concrete structures. *Materials and structures*, 44(8): 1491-1500.

[14] A. Saetta. R. Scotta., & R. Vitaliani. (1995). Stress analysis of concrete structures subjected to variable thermal loads. *Journal of Structural Engineering*, 121(3): 446-457.

[15] Lee, J H. (2012). Investigation of extreme environmental conditions and design thermal gradients during construction for prestressed concrete bridge girders. *Journal of Bridge Engineering*, 17(3): 547-556.

[16] Guan, M X. (1985). Calculation of Temperature Field, Temperature Stress and Temperature Displacement of Concrete Box Beam. *Bridge Construction*, 01: 40-49.

[17] Zhao, R D., & Wang, Y B. (2016). Studies on temperature field boundary conditions for concrete box-girder bridges under solar radiation. *China Journal of Highway and Transport*, 29(07): 52-61.

[18] Tayşi, N., & Abid, S. (2015). Temperature distributions and variations in concrete box-girder bridges: experimental and finite element parametric studies. *Advances in Structural Engineerin*g, 18(4): 469-486.

[19] Liu, Y J., & Liu, J., & Zhang, N. (2019). Review on solar thermal actions of bridge structures. *China Civil Engineering Journal*, 52(05):59-78.

[20] Peng, Y S. (2008). Studies on theory of solar radiation thermal effects on concrete bridges with application. Southwest Jiaotong University.

FINITE ELEMENT ANALYSIS FOR VIBRATION RESPONSE OF BRIDGE MODULAR EXPANSION DEVICE UNDER VEHICLE LOAD

Zhou Linren[1], Zheng Junbin[2], Zhang Haoyu[3]

[1] Associate Professor, School of Civil Engineering and Transportation, South China University of Technology, zhoulinren@scut.edu.cn.

[2] Postgraduate, School of Civil Engineering and Transportation, South China University of Technology, 1078965514@qq.com.

[3] Postgraduate, School of Civil Engineering and Transportation, South China University of Technology,

Zhanghaoyu2518@163.com

Corresponding Author: Zhou Linren, PhD, A.P.

Guangzhou, Guangdong, China, 510640

Email: zhoulinren@scut.edu.cn

ABSTRACT

Dynamic traffic load is a primary cause of damage and failure in bridge expansion joints, influencing not only the service performance of bridges but also potentially leading to traffic safety accidents on bridge decks. This study conducts a vibration response analysis of bridge modular expansion join t(MEJ) under vehicle load. Initially, the working principle, force transmission path, and boundary constraints of MEJs are analyzed to elucidate the factors influencing the vibration response and its characteristics. Subsequently, utilizing ANSYS finite element (FE) software and the APDL parametric modeling technique, a full-scale three-dimensional solid impact vibration analysis model of the MEJs is established. Then, the size, position, and duration of the dynamic traffic load on the expansion device during service are analyzed to achieve a reasonable simulation of dynamic traffic load in the FE model. Ultimately, the dynamic response of the MEJ under typical vehicle load is calculated, and the force state and vibration response characteristics of the expansion joint device are analyzed and discussed. The research methods and findings presented in this paper offer substantial theoretical calculation support for damage identification, condition assessment, and safety evaluation of MEJs.

Keywords: *Modular Expansion Joint, Vehicle Loading, Shock Vibration, Dynamic Response, Finite Element Analysis*

INTRODUCTION

Bridge expansion joints are essential components of bridges used for deformations caused by temperature changes, concrete shrinkage, creep, and uneven settlement, ensuring structural usability, safety, and travel comfort. They not only absorb bridge structure deformations but also withstand heavy vehicle loads. However, due to harsh service environments, overloads, and complex stress states, expansion joints are prone to damage or failure, often requiring replacement before reaching their design service life. For example, in the initial eight years of the Dongming Expressway in Japan, expansion joints were repaired an average of 1.6 times per joint [1]. In the United States, where the average service life of expansion joints is 10-15 years, over 250,000 out of 570,000 bridges exhibit structural defects or functional failures, with more than half of the issues attributed to deck expansion devices [2]. Despite expansion devices accounting for less than 1% of bridge construction costs, their maintenance and replacement costs surpass 20% of total bridge operation and maintenance expenses, with 16% of bridge defects occurring in these devices [3]. The primary cause of expansion joint device damage is the repeated impact dynamic load from driving rut pressure on the bridge deck. Extensive research by scholars worldwide has focused on the dynamic response analysis of bridge expansion joint devices under vehicle loads. For experimental analysis, Coelho et al. [4] carried out wheel rolling tests at various speeds on expansion joint beams with and without sliding support. Roeder [5] conducted fatigue tests measuring dynamic strain and displacement of modular expansion joint (MEJ) under vehicle action. In terms of theoretical analyses, Steenbergen [6] developed a mathematical model to study expansion joint dynamic responses, including frequency response function and impact coefficient, identifying theoretical impact coefficients exceeding 1. Yan et al. [7] investigated large displacement bridge expansion joints, establishing vertical dynamic theoretical models and calculating expansion joint vibration responses at different speeds. In numerical simulation using finite element (FE) analysis, Sun and Zhang. [8] analyzed vehicle and expansion joint models using Matlab and ABAQUS software, and derived dynamic displacement and impact coefficient values for the center beam. Ancich et al. [9] established a FE model for a single center beam and multiple supporting beams, analyzing the law of stress and strain variations under vehicle loads without considering the influence of different expansion joint widths and vehicle speeds on the dynamic response of the bridge expansion joint. Additionally, Ding et al. [10] proposed a distributed spring-damper DSD element to analyze the influence of expansion joint gap numbers and widths on vibration, while Zou et al. [11] developed a moving wheel pressure load model including vertical and horizontal components and an expansion joint FE model, presenting an analysis method for expansion device dynamic responses under combined horizontal and vertical wheel loads. Han et al. [12] analyzed expansion joint displacement responses and studied the effects of vehicle speed, vehicle-induced vibration frequency, traffic flow, and heavy vehicles on longitudinal displacement.

Dynamic response calculations based on theory models provide an important analysis method for understanding the force state and law of the expansion joint movement. However, theoretical models involve numerous assumptions and simplifications, necessitating the calculation accuracy and reliability to be improved and verified. The FE method offers a closer approximation to the actual expansion joint model. However, due to the complex structure and

force states of expansion joint devices, with the complexity of structural impact vibration calculations, current approaches mainly focus on modeling and analyzing individual components or a small number of main components. Therefore, a comprehensive FE model of the expansion joint support under vehicle load impact vibration response analysis is lacking. This paper addresses this gap by focusing on bridge MEJs. Using the FE software ANSYS, a FE modeling method of full-scale three-dimensional entity refinement is carried out for the expansion joint bearing and vibration response calculations under vehicle load impact to analyze the spatial stress states and change characteristics of MEJ and to provide technical support for expansion joint design, damage identification, and safety assessment.

BRIDGE MEJ

MEJs are widely used, with single-seam and multi-seam types. The single-seam structure is simple, while the multi-seam structure is complex and prone to damage. The structural composition of a typical multi-slot modular expansion device, shown in Figure 1, consists of three systems: support, displacement, and anchorage. As a bridge connection component, it mainly needs to meet stress and deformation requirements. When vehicles pass through the expansion device, the center beam directly bears the impact and transfers the load to the supporting beam through the sliding bearing or the connecting part. The supporting beam then transfers the load to the displacement box and anchor bar through bearings, ultimately transferring it to the bridge superstructure. During service, the bridge undergoes temperature changes, concrete shrinkage, creep, and structural deflection, causing deformation. To accommodate the deformation of the end of the bridge, the support beam can expand and contract within the displacement box along with the bridge's superstructure, thereby driving the center beam to move between the sealing belts and enabling the expansion and contraction function of the expansion device.

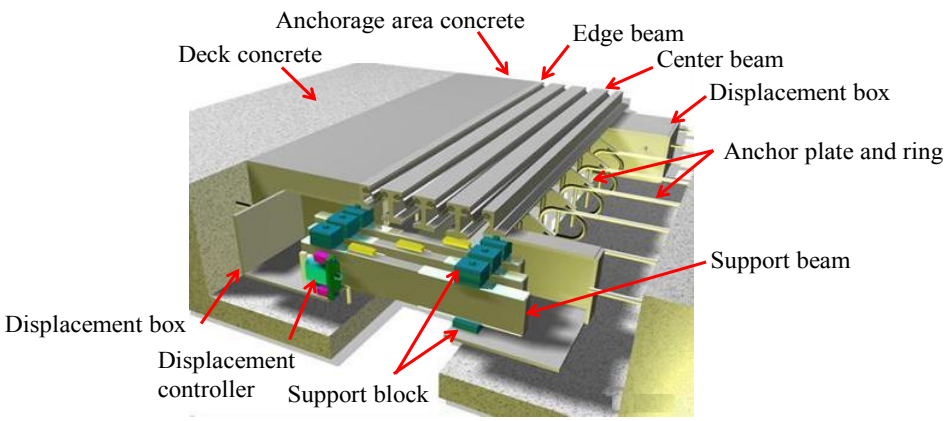

Figure 1. Three-dimensional diagram of the MEJ of bridge

FE MODELING METHOD OF MEJ FOR VIBRATION ANALYSIS

Geometries and material parameters of the MEJ

A full-scale three-dimensional solid refined impact vibration analysis model of a concrete bridge modular expansion device is established, comprising three main parts: the modular expansion device, the bridge concrete deck, and the vehicle model. The modular expansion device consists of a center beam, an edge beam, a support beam, a displacement box, and a support. Displacement boxes are spaced at 1.4 m intervals along the length direction of the expansion joint, with a total of 5 displacement boxes. The center beam, edge beam, and support beam are made of Q355 steel, the displacement box is made of Q235 steel, and the bearing and preloading support are made of cuboid blocks made from rubber and steel composite materials, with the bearing area of 70 mm × 60 mm and 70 mm × 30 mm, respectively. The bridge deck is 8.7 m long, and the width is consistent with the transverse length of the expansion device, with a thickness of 350 mm and C50 concrete. The elastic modulus of steel is 205 GPa, Poisson's ratio is 0.25, and density is 7800 kg/m^3; the elastic modulus of concrete is 34.5 GPa, Poisson's ratio is 0.2, and density is 2600 kg/m^3. The vehicle model consists of a two-axle vehicle with tire dimensions of 650 mm, a wheelbase of 2.8 m, and a tire spacing of 1.8 m.

Element types for the FE model

The FE calculation model of the modular expansion device is established using ANSYS software, incorporating four types of elements: solid element SOLID65, CONTA174/TARGE170 contact element, spring element COMBIN14, and mass element MASS21. SOLID65 is an element used for three-dimensional solid modeling of concrete structures, which feature eight nodes with three translational degrees of freedom per node and no rotational degrees of freedom. CONTA174 is an 8-node element utilized to represent contact and slip between 3D target surfaces and deformable surfaces (flexible surface), enabling 3D structural and thermal-structural coupling contact analysis. TARGE170 is commonly used to represent three-dimensional target surfaces associated with various contact elements (CONTA173, CONTA174). The contact element overlays the solid element describing the boundary deformation body and may come into contact with the target surface defined by the TARGE170 element. COMBIN14 is used to set the suspension equivalent spring connection effect of the vehicle, while vehicle mass is added by MASS21. MASS21 is a point-cell type with six degrees of freedom, allowing for different masses and moments of inertia in each direction.

FE modeling method of MEJ for vibration analysis

APDL (ANSYS Parametric Design Language) is a scripting language used to perform routine finite element analysis operations or to analyze models by means of parametric variables. The programming language allows users to organize ANSYS commands to implement finite element analysis. The APDL-based parametric 3D solid modeling method is adopted. The element types used include SOLID65 solid unit, CONTA174/TARGE170 contact unit, TARGE17 contact slip element, spring element COMBIN14 and mass element MASS21. According to the actual size of each component of the MEJ device, the SOLID65 solid unit is used to establish the center beam, edge beam, support beam, penetration weld, displacement box, anchoring area concrete, pressure bearing and precompression support block.

Corresponding material properties are set to elements of these components. The components embedded in each other are connected by common nodes on the connecting interfaces. Contact elements and slip elements are used to simulate the corresponding constraints and slip between the components with contact slip. The contact slip mode is adopted for the connection between the support blocks and other components. The solid model of tire ring entity is established according to the determined vehicle parameters, and the inner surface of the tire entity is translationally connected with the equivalent node of the tire center, so that the tire can drive forward and roll freely. A contact pair is created between the outside surface of the tire and the upper surface of the bridge deck to achieve a rolling effect with friction through a standard contact type. The end of the bridge deck is fixed constrained, and the vertical displacement of bridge deck is constrained. The established full-size 3D solid refined shock and vibration analysis model is shown in Figure 2. The entire model includes 130,125 element s and 155,203 nodes.

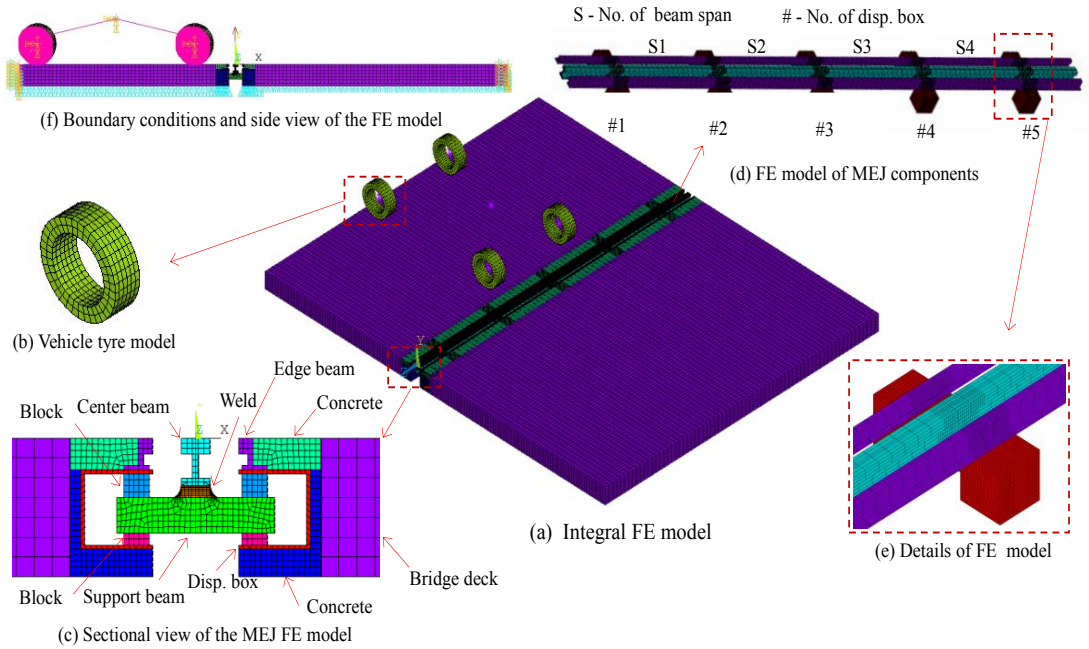

Figure 2. FE model for impact vibration analysis of MEJ

Model characteristics

This paper proposes a refined modeling method for the impact model of the MEJ device, employing parameterization to set the model size for quick adjustment of component sizes and facilitate parametric analysis. Seam width is also set by parameterization, enabling adjustment for different expansion device working states. A length of the bridge deck is established, considering its influence on expansion joint restraint stiffness through boundary constraints. The penetration weld is used between the center beam and main beam to ensure force transmission and stress state consistency with the actual project. A vehicle model is created to

accurately simulate real driving conditions, with vehicle speed, mass, wheelbase, etc., set as parameters for efficient application or modification of vehicle loads.

FE SHOCK VIBRATION ANALYSIS FOR BRIDGE MEJ

Vehicle dynamic load

According to codes of China, *General Code for Design of Bridges and Culverts* (JTGD60-2015), and other design specifications, this paper establishes a two-axle vehicle model. The vehicle has a wheelbase of 2.8 m, a mass of 2.5 t, and a speed of 100 km/h, considering the speed limit. The tire radius is defined as 65 cm. The paper analyzes the vibration response of the modular expansion device of the large displacement bridge under vehicle load. The vehicle load is arranged according to the most unfavorable situation, as illustrated in Figure 2. One wheel load acts on the middle of the second span of the center beam, and the other wheel load acts on the third span of the center beam according to the transverse wheelbase.

Dynamic responses of MEJ under vehicle action

Stress

When the front wheel applies pressure to the center beam, the overall structure experiences its highest stress, with the maximum stress distribution depicted in Figure 3. The maximum stress occurs at the weld joint between the center beam and the support beam of the 3rd displacement box, measuring 12.16 MPa. In practical engineering, the dynamic traffic load induces stress concentration at the weld connection interface between the center beam and the support beam of the expansion device, making it prone to cracking and gradual deterioration until the connection is damaged.

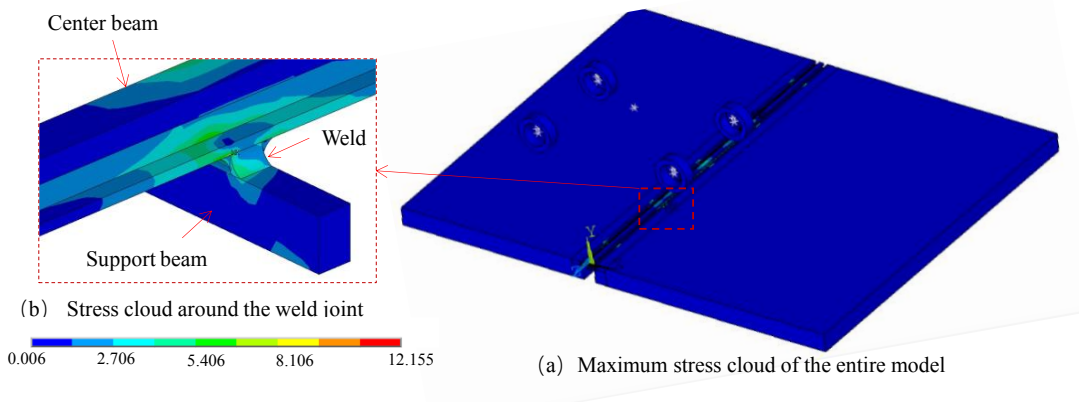

Figure 3. Stress (MPa) distribution of MEJ under vehicle loading

Displacement

When the front wheel presses on the center beam, the overall structure experiences its maximum deformation, with the distribution of the maximum deformation shown in the figure (the nephogram results include the vehicle weight). The displacement deformation of the center beam in the expansion joint device is most prominent, with the maximum vertical downward displacement of approximately 0.0625 mm, aligned with the vertical load of the wheel. This displacement occurs in the middle of the second span of the Figure 1 beam under the wheel load. The adjacent first span of the Figure 1 beam experiences upward displacement, with a maximum displacement of about 0.01 mm. The load affects the middle of the second span and part of the third span, with the middle of the second span of the center beam bearing the highest load. This paper establishes an impact vibration analysis model of the MEJ device, and the calculated displacement accurately reflects the actual deformation of the expansion joint device.

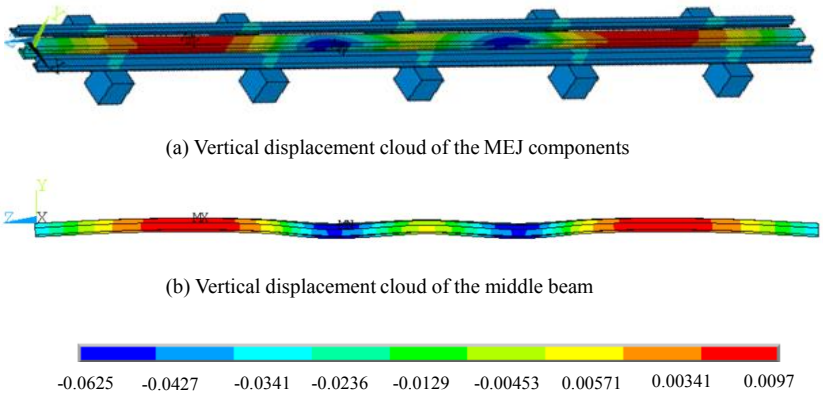

Figure 4. Vertical displacement (mm) of the MEJ under vehicle loading

Dynamic responses of the expansion device under vehicle action

Dynamic traffic load is a primary cause of bridge expansion joint device damage. Vehicle load, tire type, wheelbase, and driving speed substantially impact the forces of the expansion joint device. Based on the established full-size FE model, the dynamic response of the MEJ device under the dynamic action of the moving vehicle load is calculated. The vehicle load model has a mass of 2.5 t, a front and rear wheelbase of 2.8 m, a left and right wheelbase of 1.8 m, a tire radius of 650 mm, a tire width of 205 mm, and a vehicle speed of 100 km/h. The stress, displacement, and vibration response of the beam, crossbeam, and edge beam in the expansion joint under dynamic vehicle loads are analyzed.

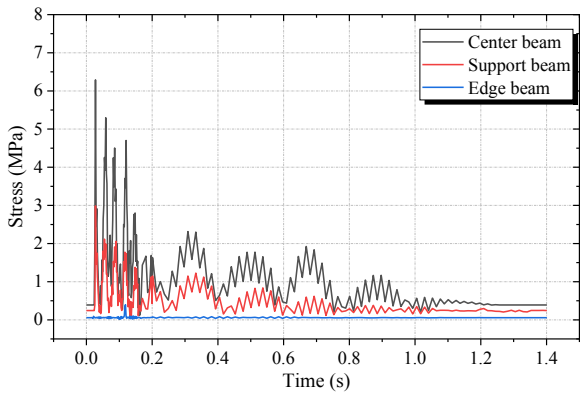

Figure 5. Dynamic stress responses of expansion joint members

The stress response of the center beam, crossbeam, and edge beam in the expansion joint under traffic load is illustrated in Figure 5. The stress response of the center beam and crossbeam is prominent, with maximum stress distributions of 6.2 MPa and 3.0 MPa, respectively, occurring when the front wheel contacts the center beam of the expansion joint. The stress response of the component is more intense within the first 0.2 s, with stress periodically and continuously attenuating in 0.2 s-1.2 s, and dynamic stress response usually attenuating around 1.2 s. The dynamic strain characteristics of the center beam and crossbeam directly impact the fatigue damage of components. In contrast, the dynamic stress of the boundary beam is relatively low due to complete anchoring to the bridge concrete, providing strong boundary constraints and stiffness.

Displacement

The dynamic displacement response of the center beam, crossbeam, and edge beam of the expansion joint under the action of traveling vehicle load is shown in Figure 6. Displacement response is more prominent within the first 0.2 s, periodically decaying between 0.2 s-1.0 s, with dynamic displacement nearly reaching 0 after 1.0s. The most prominent dynamic displacement occurs in the center beam, reaching a maximum value of 0.074 mm, representing vertical downward displacement when the front wheel first contacts the center beam. The dynamic displacement of the crossbeam follows a similar trend to that of the center beam but is relatively smaller, with a maximum value of about 0.01 mm, due to its greater stiffness compared to the center beam. The dynamic displacement response of the edge beam is almost zero because it is anchored to the bridge deck, and the vertical stiffness of the bridge deck fully restrains it in this model, resulting in a very large vertical stiffness of the edge beam.

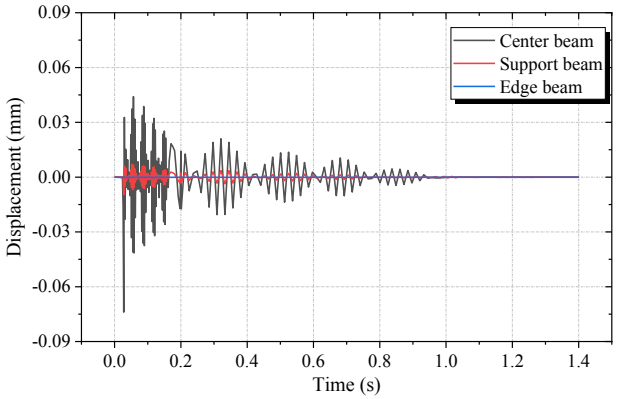

Figure 6. Dynamic displacement responses of expansion joint members

The dynamic response of the expansion joint device under traffic load mainly occurs in the center beam and crossbeam components, exhibiting different response magnitudes and stiffness levels. The center beam has relatively lower stiffness, but the dynamic strain and displacement are the largest, which is also the fundamental reason making it prone to damage in practical engineering. The dynamic response of the center beam and crossbeam shows a considerable low-period oscillatory decay after 0.2 s because the vehicle remains on the model deck for approximately 0.2 s, after which the expansion joint device undergoes damped free decaying vibration without external excitation.

CONCLUSION

Based on FE analysis, a study on the 3D entity refined modeling method of the MEJ device is proposed and conducted. Dynamic calculation and analysis of the bridge expansion joint device under vehicle load are performed, leading to the following main conclusions:

(1) The main parameters and control variables of the model can be quickly adjusted using the full-size parametric three-dimensional entity modeling method. This method establishes a full-size three-dimensional entity refined model of the MEJ impact model, accurately reflecting characteristics of the expansion joint such as the actual structure, force transfer path, contact slip, and boundary constraints. It effectively simulates the working and stress state of the expansion joint in actual engineering.

(2) A 3D solid vehicle modeling method is proposed, parameterizing vehicle mass, wheelbase, and driving speed. This approach effectively simulates actual vehicle driving and impact modes, enabling rapid adjustment and efficient application of vehicle loads.

(3) Under the load of the vehicle traversing the expansion device at an unfavorable position, the stress state of the MEJ device at the connection point of the center beam and crossbeam is highly complex and unfavorable. Substantial stress concentration occurs at the weld, making it a major factor contributing to crack damage and failure in actual projects. The center beam, edge beam, support beam, and other components exhibit noticeable dynamic

responses during vehicle load, with the center beam and support beam experiencing larger dynamic responses lasting less than 2 seconds.

(4) When the vehicle passes through the expansion device at an unfavorable position, noticeable deformation occurs in the center beam of the modular expansion device, and deformation in other components and concrete in the anchorage zone is small. The maximum vertical displacement of the center beam is about 0.0625 mm, with a maximum rebound displacement of about 0.0562 mm. Center beam deformation aligns with the response characteristics of impact vibration and remains within the allowable range.

ACKNOWLEDGMENTS

This work is supported by the National Natural Science Foundation of China (52078220), the International Science & Technology Cooperation Program of Guangdong Province (2023A0505050155) and the International and Hong Kong, Macao and Taiwan Talents Communication Program of Guangdong Province.

REFERENCES

[1] Peng, D. W., Lin, Z. P., & Hong X. J. (2006). Research and Practice of Jointless Bridges. *Highway*, 08,53-62.

[2] Zhang, Y. F., Chen, F. X., Zhang, L. T., et al. (2013). Condition analysis and handling measures for expansion joints of long span suspension bridges. *Bridge Construction*, 43(05),49-54.

[3] Xiao, B., Xu, W. B., Yang, X. Y., et al. (2021). Research overview of bridge expansion joint' disease and its influence. *Journal of Disaster Prevention and Mitigation Engineering*, 41(01),167-180.

[4] Coelho, B. Z., Vervuurt, A. H. J. M., Peelen, W. H. A., et al. (2013). Dynamics of modular expansion joints: The martinus nijhoff bridge. *Engineering Structures*, 48, 144-154.

[5] Roeder, C. W. (1998). Fatigue and dynamic load measurements on modular expansion joints. *Construction and Building Materials*, 12(2-3), 143-150.

[6] Steenbergen, M. J. (2004). Dynamic response of expansion joints to traffic loading. Engineering structures, 26(12), 1677-1690.

[7] Yan, Q. M., Wang, S. H., Yang, G. et al. (2013). Research of vertical dynamic response of the large displacement bridge expansion joint. *Machinery Design Manufacture*, 07, 41-43+46.

[8] Sun, Z., & Zhang, Y. F. (2014). Vehicle-induced dynamic response of expansion joints in long span bridges. *Applied Mechanics and Materials*, 584, 2117-2120.

[9] Ancich, E. (2007). Dynamic design of modular bridge expansion joints by the finite element method. IABSE REPORTS, 93, 304.

[10] Ding, Y., Zhang, W., & Au, F. T. (2016). Effect of dynamic impact at modular bridge expansion joints on bridge design. *Engineering Structures*, 127, 645-662.

[11] ZOU Y. Y., Lu J. P., Ding, Y., et al. (2019). Computation of dynamic strength of modular bridge expansion joint and analysis of influencing factors. *Journal of Ningbo University* (NSEE), 32(01), 72-79.

[12] Han, D. Z., Guo, T., Huang, L. Y., et al. (2019). A study on longitudinal displacements and damage control of expansion joints of long-span steel bridges under stochastic traffic loads. Journal of Vibration and Shock, 38(24), 172-178.

EXPERIMENTAL STUDY ON SEISMIC PERFORMANCE OF ASSEMBLED PIERS WITH EXTERNAL CORRUGATED STEEL PLATES

Shuangshuang Jin[1], Shiyu Zhou[2], and Jianting Zhou[3]

[1] Professor, Chongqing Jiaotong University, jinshuangshuang@cqjtu.edu.cn.

[2] Postgraduate, Chongqing Jiaotong University, 920000648@qq.com.

[3] Professor, Chongqing Jiaotong University, jt-zhou@163.com.

Corresponding Author: Shuangshuang Jin, Professor.

Chongqing, China, 400074

Email: jinshuangshuang@cqjtu.edu.cn

ABSTRACT

Based on the design concept of concentrated energy consumption and replaceability, a prefabricated segmental assembled pier with external replaceable corrugated steel plate is proposed. The tenon and mortise of the embedded steel pipe is used as the shear connection. To verify the replaceability of prefabricated bridge piers, the pier specimen with perforated corrugated steel plates as energy dissipation components was designed and manufactured. First, the fatigue loading test was conducted on the specimen. After the test, the damaged corrugated steel plate was replaced by a new one, and then a quasi-static reciprocating loading test was conducted. The results show that the assembled pier with replaceable corrugated steel plate is capable of providing high energy dissipation. The mortise and tenon of embedded steel pipe limit the relative dislocation between segments and improve the shear capacity of the structure at the segmental connection effectively. Since the energy consumption of the bottom concrete section is mainly concentrated on the external corrugated steel plate, there is no crushing failure and damage of the bottom concrete section during the test. The external corrugated steel plate can achieve replaceable performance under the design target drift rate, which can be used in engineering structures.

Keywords: *Precast assembled pier, Corrugated steel plate, Pseudo-static testing, Replaceability, Hysteretic behaviour*

1. INTRODUCTION

To implement the accelerated bridge construction (ABC), prefabricated assembly technology has been developed greatly in recent years [1]. The bridge substructure using prefabricated assembly technology can speed up the construction speed and reduce environmental pollution, which is similar to cast-in-place piers in terms of damage to pier bottom, but in terms of structural integrity and energy consumption capacity is not as good as traditional cast-in-place

piers. Therefore, many researchers have done research on the problems of serious damage at the bottom of assembled bridge piers and poor energy dissipation capacity.

For the assembled bridge piers, their energy dissipation capacity is weak, which can be enhanced by using internal and external energy dissipation devices. Ou et al. [2] proposed that precast segmental bridge piers incorporate energy dissipating reinforcement to improve the energy dissipation capacity. Billington et al. [3] used a ductile fiber-reinforced cement-based composite in the precast segments at potential plastic hinging regions. Marriott et al.[4] improved the energy dissipation capacity of bridge piers by using integral prefabricated bridge piers with external, fully replaceable, mild steel hysteretic dissipaters at the bottom of the piers, and verified by quasi-static tests. ElGawady et al. [5] used angle steel and energy dissipation steel bar devices at the bottom of the pier, connected to the embedded parts by high-strength bolts. Han et al. [6] installed a replaceable post-earthquake buckling restrained energy dissipation device around the bottom of the pier. Jia et al.[7] used energy dissipation steel plates, anti-buckling cover plates, gaskets and connecting bolts to form a complete energy dissipation device in the plastic hinge area at the bottom of the pier based on the actual project, and verified the feasibility of this design method through quasi-static loading test.

In this paper, a novel assembled bridge pier structure with external perforated corrugated steel plates as the concentrated energy dissipation component of the plastic hinge region at the pier bottom was proposed. To verify the replaceability of prefabricated bridge piers, The low-cycle fatigue loading test and quasi-static cyclic loading test of a group of specimens were carried out to study the bearing capacity, ductility, deformation, and hysteretic energy dissipation of specimens.

2. PIER WITH PERFORATED CORRUGATED STEEL PLATES

Figure 1 shows the general structure of the assembled pier with external perforated corrugated steel plates. The pier is connected to the upper and lower sections of the structure by external perforated corrugated steel plates, which are also used as energy dissipation components at the bottom of the assembled pier. The assembling process of this bridge pier is that the foundation, bottom concrete section and upper concrete section are assembled in sequence. The perforated corrugated steel plates on both sides are connected to the perforated L-shaped connectors located at the top and the bottom by high strength bolts. Then the upper and lower steel pipe tenon embedded parts are inserted into the pre-drilled aperture of the bottom section as a shear resistance system at the joint of the assembled section. In order to enhance the force transmission efficiency of the structure, two vertically placed steel plates are added to the position of the upper section embedded parts welded with the force longitudinal reinforcement, and they are welded to the embedded parts first and then to the force longitudinal reinforcement. Thus, the upper concrete section reinforcement skeleton and embedded parts form a monolithic structure. In order to give full play to the role of the transverse reinforcement inside the foundation slab and improve the integrity of the embedded parts and the foundation slab. The transverse reinforcement in the foundation slab partially crosses the vertical welded perforated connecting plate of the embedded parts of the foundation slab and cast-in-place with the foundation slab to form a stress body.

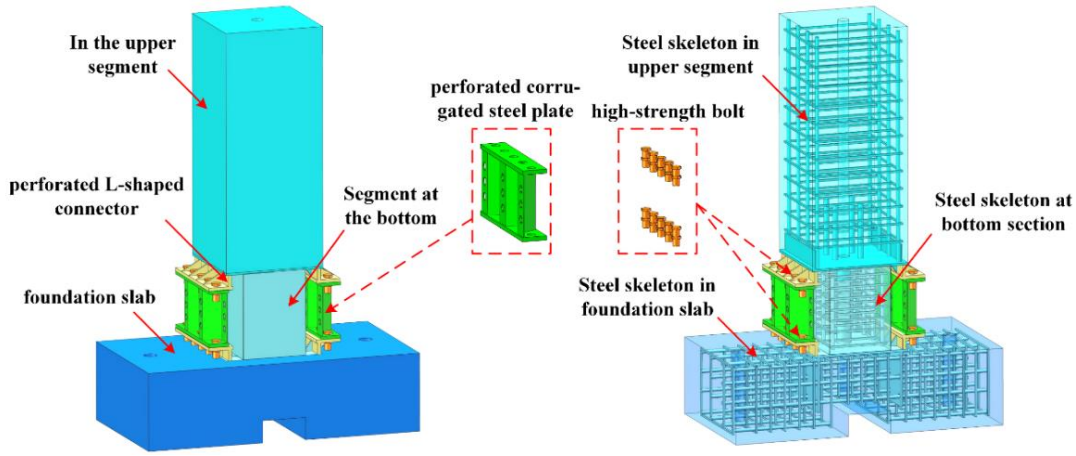

Figure 1. Fabricated bridge piers with external perforated corrugated steel plates

3. SPECIMEN DESIGN

In order to verify the effectiveness of energy dissipation centralized and replaceable devices. The detailed design of the specimen is shown in Figure 2.

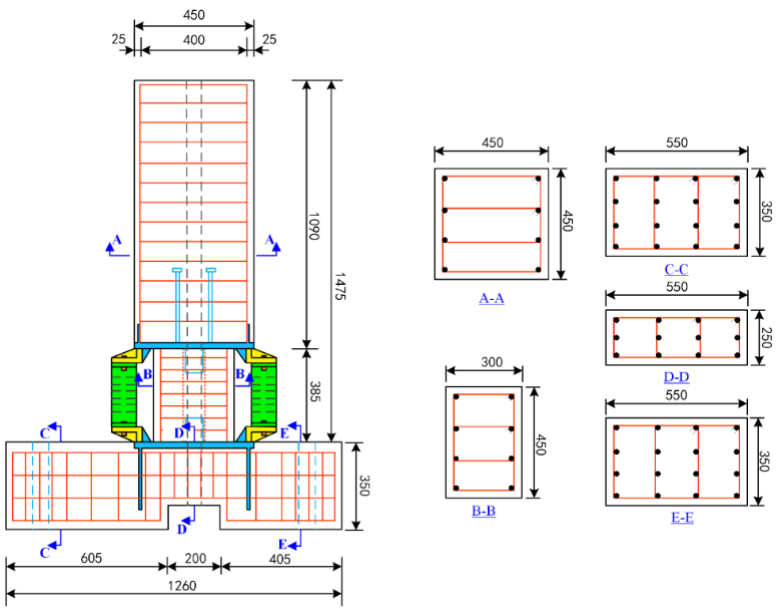

Figure 2. Details of the specimen (units: mm)

The specimen was designed and fabricated using the scaled model. The specimen is prefabricated in two sections. The size of the upper segment is 450mm×450mm×1090mm, the size of the lower segment is 300mm×450mm×385mm, the size of the foundation slab is

1260mm×550mm×350mm, the length of the welded steel pipe tenon joint is 100mm, the diameter is 50mm, and the wall thickness is 2.5mm. In order to facilitate the connection between the corrugated steel plate and the upper and lower prefabricated parts. The connecting plates of L-type connectors and corrugated steel plates are each perforated with a total of 20 holes. The diameter of the hole is 30mm, and the connection is made with 10.9 grade M27 bolts. The initial design parameters of the specimens include: C40 concrete material, 25mm protective layer thickness, Q345 steel for the embedded parts, Q235 steel for the energy dissipation perforated corrugated steel plates, 8mm diameter HPB300 rebars for the stirrup.

The specimen was first subjected to the low-cycle fatigue loading test during the test process, with the aim of examining the replaceable performance of the specimen at 2% of the design target drift ratio, the fatigue loading is shown in Figure 3a. Then the specimen with the external energy dissipation component replaced was subjected to the quasi-static cyclic loading test (the loading as shown in Figure 3b) to study whether the external energy dissipation component could realize the concentrated energy dissipation and the seismic performance of the specimen. There was no axial load applied on the specimen.

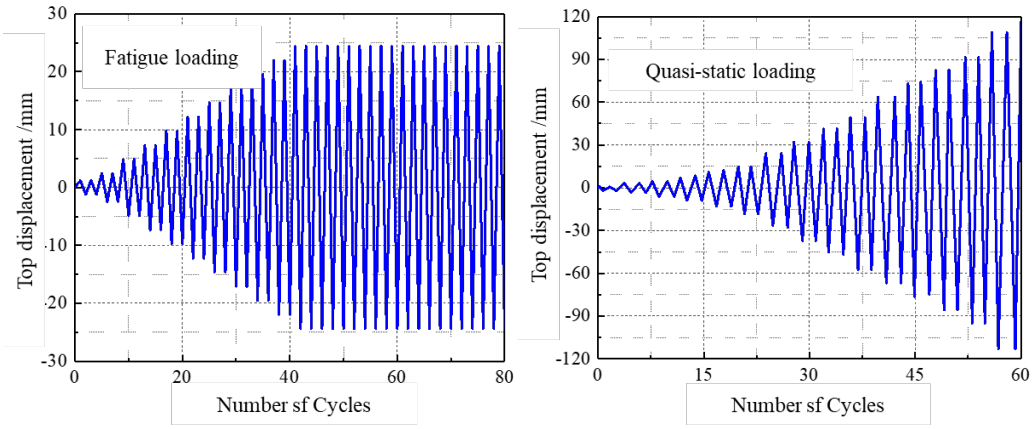

(a) Fatigue loading (b) Quasi-static loading

Figure 3. Photograph of the specimen prior to testing

4. TEST RESULTS

4.1. Low cycle fatigue loading test of the specimen

Figure 4 shows the photograph of the specimen prior to testing. The design target drift ratio of 2% is used as the control displacement for the low-cycle fatigue loading test.

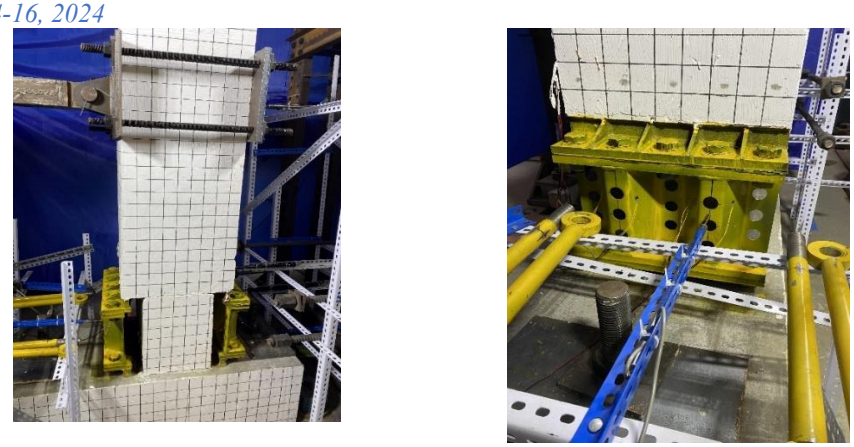

Figure 4. Photograph of the specimen prior to testing

During the loading process, the strain gauge data on the energy dissipation components were observed in real time. Before loading to the design target drift ratio, the strain on the energy dissipating members increased steadily. The left perforated corrugated steel plate reaches yield at the first positive loading cycle when the design target drift ratio is reached. The right perforated corrugated steel plate also yielded during the subsequent negative loading of the same level. During the low-cycle fatigue loading process, a total of 70 cycles was applied to the specimen at the drift ration of 2.0%, and the test was terminated when the load capacity of the specimen decreased to 80% of the peak load capacity. The crack development and hysteresis curves are shown in Figures 5 and 6. From the figures, it can be seen that the specimen maintains good integrity and the concrete crack development is mainly concentrated at the joint between the embedded parts and the concrete, and the crack development is slight. In addition, the deformation of the embedded parts is very small, and they are all in the elastic stage, which meets the replaceability of the subsequent energy-consuming members.

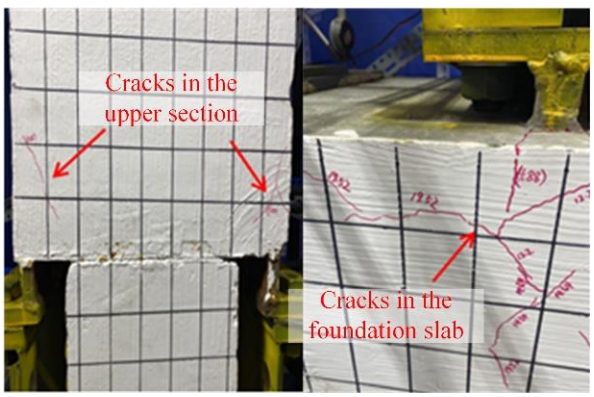

Figure 5. Cracks in the specimen

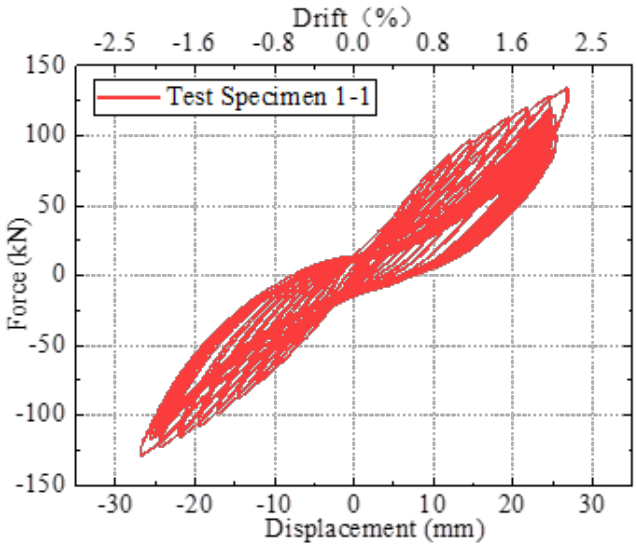

Figure 6. Load-displacement hysteresis curves of the specimen

4.2. Replaceable capacity of the specimen

For the specimen, the small concrete cracks produced during the low-cycle fatigue loading test were repaired by concrete crack repair agent for strength. The replacement process of the specimen is shown in Figure 7.

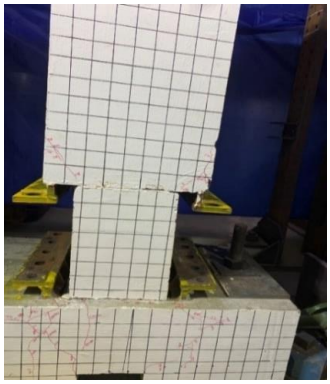

(a) Remove external energy dissipation components of the specimen

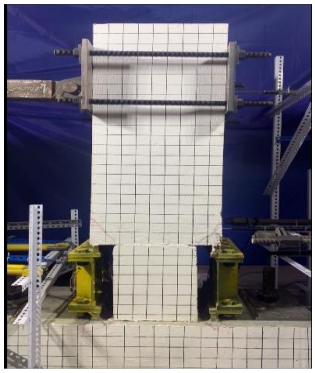

(b) The specimen after replacing the energy dissipation components

Figure 7. Replacement process of external energy dissipation components

After the crack repair and the replacement of the external energy dissipation components, the specimen was subjected to the quasi-static test. The crack development and deformation of the specimen in the first period were basically the same as the fatigue loading test phenomenon. With the increasing loading level, the concrete cracks on the upper section gradually developed

upward, there is minor damage on the bottom concrete section, and the concrete cracks on the bearing platform extended symmetrically all around. When the displacement of the pier is loaded to 48.8mm (drift ratio 4%), the external perforated corrugated steel plates appear buckling deformation in the front and rear edges. Moreover, the deformation of the external perforated corrugated steel plates in the strong plastic stage alternated with the loading direction.

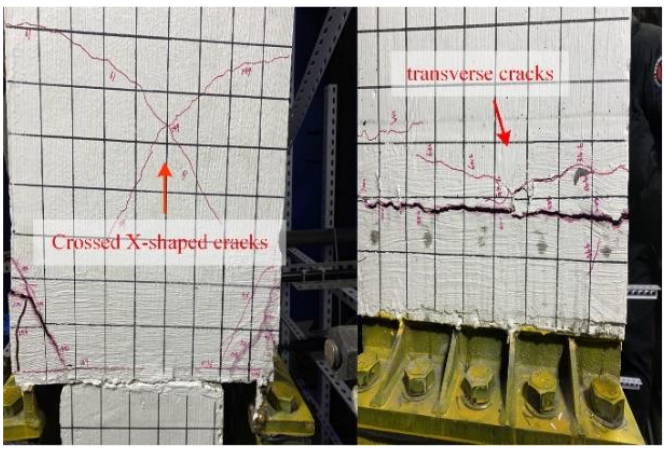

Figure 8. Cracks in the specimen

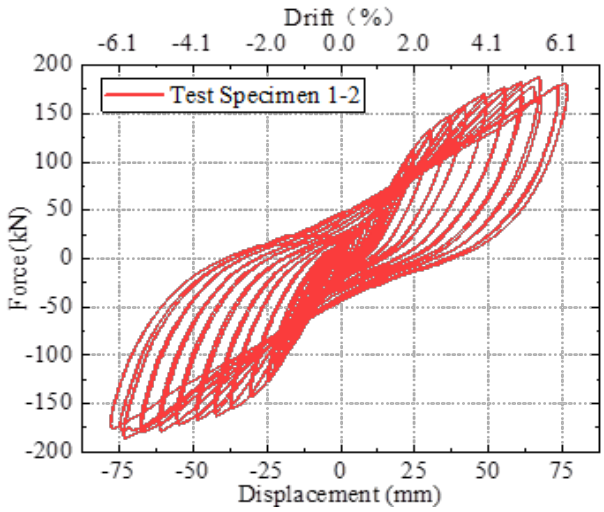

Figure 9. Load-displacement hysteresis curves of the specimen

The test phenomena of the specimen under subsequent loading levels are basically the same. One of the main phenomena is that buckling deformation of the external dissipation perforated corrugated steel plates alternately repeat with the loading displacement left and right. The overall cracks, deformation development and force-displacement curves of the specimen are shown in Figures 8 and 9, respectively. It can be seen that the deformation of the embedded

part of the specimen is still very small. The external energy dissipation component has entered the strong plastic stage. The concrete damage at the joint between the upper section embedded parts and concrete is large. From the hysteresis curves, the overall energy dissipation capacity of the specimen has been improved after external perforated corrugated steel plates have entered the strong plastic stage, and the specimen after replacing the energy dissipation components has good ductility.

5. CONCLUSIONS

This paper firstly proposes a fabricated bridge pier with external perforated corrugated steel plates as centralized energy dissipation and replaceable device in the plastic hinge area at the pier bottom. A specimen was designed and fabricated for low cycle fatigue and quasi-static loading tests. The external corrugated steel plate can achieve replaceable performance under the design target drift ratio.

ACKNOWLEDGMENTS

This study was supported by the National Natural Science Foundation of China (Grant No. 52078092), and the Chongqing Natural Science Foundation Innovation and Development Joint Fund (2022NSCQ-LZX0146). Their financial support is gratefully acknowledged.

REFERENCES

[1] Hewes J T. (2002). *Seismic design and performance of precast concrete segmental bridge columns*. University of California, San Diego

[2] Ou Y C.(2007). *Precast segmental post-tensioned concrete bridge columns for seismic regions*. State University of New York at Buffalo.

[3] Billington S L, Yoon J K. (2004). Cyclic response of unbonded posttensioned precast columns with ductile fiber-reinforced concrete. *Journal of Bridge Engineering*, 9(4): 353-363.

[4] Marriott D, Pampanin S, Palermo A. (2009). Quasi-static and pseudo-dynamic testing of unbonded post-tensioned rocking bridge piers with external replaceable dissipaters. *Earthquake engineering & structural dynamics*, 38(3): 331-354.

[5] ElGawady M A, Sha'lan A. (2011). Seismic behavior of self-centering precast segmental bridge bents. *Journal of Bridge Engineering*, 16(3): 328-339.

[6] Han Q, Jia Z, He W et al. (2017). Seismic Design Method and Its Engineering Application of Self-centering Double-column Rocking Bridge. *Zhongguo Gonglu Xuebao/China Journal of Highway and Transport*, 30(12): 169-177

[7] Jia J, Wei B, Ou J et al. (2021). Tests for seismic performance of prefabricated self-centering bridge piers with external replaceable energy dissipator. *Journal of Vibration and Shock*, 40(05): 154-162.

BEHAVIOR OF HOLLOW STEEL TUBULAR COLUMNS SUBJECTED TO LOW-VELOCITY LATERAL IMPACT BY DEFORMABLE PROJECTILE: NUMERICAL STUDIES

Prithvi Sangani[1], Kaushik Ghoshal[2], and Anil Agarwal[3]

[1] Research Scholar, Indian Institute of Technology, Hyderabad, ce20resch13001@iith.ac.in.

[2] Scientist-F, Research Center Imarat, DRDO, kaushik.ghoshal.rci@gov.in

[3] Associate Professor, Indian Institute of Technology, Hyderabad, anil@ce.iith.ac.in

Corresponding Author: Prithvi Sangani.

IIT Hyderabad Kandi(M), Sangareddy Dist-502 284 Telangana, India

Email: ce20resch13001@iith.ac.in

ABSTRACT

Steel tubular sections are frequently used in modern construction due to their structural efficiency and aesthetic appearance. In current defense operations, low-velocity projectiles are employed to neutralize enemy targets within buildings. The current challenge is to evaluate the damage caused by the low-velocity projectile, ensuring it does not inflict significant structural damage to the building while maintaining its ability to neutralize enemy targets. To assess the stability of a building, it is crucial to study the stability of columns. This study focuses on investigating the combined axial load and lateral impact of low-velocity projectiles (AA 2014-T6) on steel columns through various numerical analyses. The numerical model developed was calibrated with the existing experiments in the available literature that mostly focussed on rigid impactors. Johnson-Cook model parameters available in the literature were imported to Abaqus for numerical analyses, and models were created using a projectile of mass 26.5 kg with an impact velocity of 20m/s. The model was analyzed by varying parameters such as column thickness, the cross-sectional shape of the column, the axial load level, and the projectile mass distribution. The results showed that as the column thickness increases, the deformation of the projectile increases while the out-of-plane deformation of the column decreases. However, the deformation of the column increases with an increase in axial load level. Additionally, the effect of mass distribution in the projectile has a limited influence on the overall deformation of the projectile.

Keywords: *AA 2014-T6, Deformable projectile, Johnson-Cook model, Low-velocity impact, Numerical modeling, Steel tubular columns*

INTRODUCTION

Low-velocity projectiles are increasingly being employed in modern day defense operations due to their effectiveness in neutralizing hostile targets within buildings while minimizing structural damage. An important challenge in such is evaluating the damage caused by these projectiles to strike a balance between neutralizing threats and preserving the structural stability of buildings. The present study particularly focuses on the stability of columns, which play a critical role in maintaining the overall structural integrity of buildings. Aluminum alloys are highly utilized in industries like aerospace, defense, and automobiles because of their exceptional properties, such as a high strength-to-weight ratio, resistance to corrosion, lack of flaking, and high fracture resistance [1]. Among these alloys, AA2014-T6 is notable for its superior strength compared to others, making it an ideal choice for applications like airframes in the defense sector. In parallel, the use of steel tubular sections in modern construction has increased significantly due to their structural efficiency and aesthetic appeal [2,3]. Defining low-velocity and high-velocity impacts remains a challenge, as different studies propose varying velocity ranges. For instance, some studies [4] consider velocities from 0.5 to 34.2 m/s as low velocities, while others [5] extend this range up to 50 m/s. In the context of this study, a low-velocity impact is defined with a projectile velocity of 20 m/s.

The use of numerical simulations is favored over experimental analysis for impact problems due to cost and time constraints. However, the precision and reliability of these simulations rely on selecting suitable constitutive models that effectively depict the mechanical properties of materials. Among the range of available models, the Johnson-Cook model was preferred for its simplified formulation and the reduced necessity for experimental tests to determine its parameters.

W Li et al. [6] in their paper investigated the response of Ultra High Strength Steel (UHSS) hollow tubes to low-velocity lateral impact loading through experimental and numerical analyses. Impact tests are conducted using a falling-weight impact test machine, and results such as failure modes, impact force, and specimen deformation are recorded and analyzed. A corresponding Finite Element (FE) model is developed and validated against experimental data. The present study develops the FE model and validates the results of FE model developed by W Li et al.[6]. The numerical models are designed to vary certain parameters systematically during the analysis. These parameters include the thickness of the columns, the cross-sectional shape of the columns, the direction of impact, axial load levels applied to the steel columns, and the resulting damage observed in both the column and the projectile. By exploring these variations, the study aims to gain insights into how different factors influence the structural response and damage mechanisms when subjected to low-velocity impacts.

VALIDATION STUDIES

W. Li et al.[6] conducted a series of tests involving six specimens subjected to lateral impact loading. They have developed a finite element (FE) model considering the strain rate effect and subsequently validated it against experimental results. Their study utilized a rigid impactor for

the tests. The current research, focusing on numerical analysis, aims to validate their findings to extend the study by parametric analysis of deformable projectile impact. The specimen details were outlined in their paper [6], with specifics such as the diameter (D), thickness (t), and length (L_e) of the specimen provided in Table 1. The study also investigated the influence of axial load level (n) on the impact force. Using the same material properties and the FE model with a rigid impactor in our simulations, the results were tabulated for comparison. This comparison primarily focussed on the maximum impact force (F_m) and maximum displacement (Δ_m) between the experimental and numerical analyses.

W. Li et al. reported mean values of 1.05 for both maximum force and maximum displacement in comparison to the experimental observations. In the present study, the analysis yielded mean values of 0.95 and 0.96 for maximum force and maximum displacement, respectively. In this study, the clamps that hold the column in W Li et al.'s paper [6] were not modeled. Instead, a boundary condition at the ends of the columns was provided as a fixed boundary condition except for axial displacement to introduce axial load level. Consequently, this makes the model in the present system slightly rigid in comparison to W Li et al.'s [6] simulations. In W Li et al's [6] simulation, the column and clamps were tied by defining interaction. This approach might introduce flexibility into the system, thus making the estimates conservative in the case of W Li et al.'s simulation. However, for the parametric analysis, W Li et al. [6] have considered defining boundary conditions on the column ends. These results indicate that the developed numerical model tends to slightly overestimate both maximum impact force and maximum displacements when compared to the experimental data.

Table 1. Specimen details and comparisons of W Li et al. [6] and present study

					W Li et al. [6]		Present study	
Speci-men	D(mm)	L_e(mm)	t(mm)	n	F_m: measured/ predicted	Δ_m: measured/ predicted	F_m: measured/ predicted	Δ_m: measured/ predicted
T-1	31.8	480	1.75	0.3	1.12	1.05	0.89	0.93
T-2	31.8	480	1.75	0.3	0.86	1.12	0.94	1.11
T-3	31.8	480	1.75	0.3	0.90	1.07	0.94	1.07
T-4	38.1	640	1.90	0	1.13	1.04	1.00	0.86
T-5	38.1	640	1.90	0.3	1.21	1.03	0.96	0.89
T-6	38.1	640	1.90	0.6	1.08	0.98	0.95	0.89
			Mean		1.05	1.05	0.95	0.96
			COV		0.12	0.04	0.04	0.10

NUMERICAL MODELING

The present study involves the analysis of two distinct types of structural columns: a circular column with an outer diameter of 200mm and a square column with a side length of 220mm. The chosen length for both columns is 3600mm, which aligns with typical dimensions found in residential construction. The material selected for these columns is Yst 310, which has an yield stress of 460 MPa.

The projectile measures 1500mm in length and comprises a cylindrical tube with a diameter of 140mm and a wall thickness of 1.5mm. Additionally, the hemispherical head of the projectile possesses a 3mm thickness. To simulate the weight distribution of the projectile's components, equivalent weights of steel discs were placed at the center of mass for each segment. This reflects the total mass of the projectile, which amounts to 26.5 kilograms. The material selected for the projectiles was AA 2014-T6, which has a yield stress of 423 MPa. The velocity of impact for the projectile is considered as 20m/s, a parameter crucial for evaluating its structural response and performance characteristics. The detailed schematic illustrating the components of the projectile is provided in Fig.1.

The model employed in this study utilizes numerical analysis within the ABAQUS/Explicit [7] module. As illustrated in Fig. 2, a model has been developed to represent the steel tubular column and the AA 2014-T6 projectile. Optimal mesh size was obtained by mesh convergence studies for accuracy and computationally efficient results. Rate dependent material properties were incorporated into the numerical analysis and the material properties obtained through material characterization reported in Sangani et al. [8] have been incorporated into the analysis. The Johnson-Cook parameters considered are tabulated in Table 2. For both the column and the projectile, the type of elements considered in this study was S4R, which was successfully employed by W. Li et al. [6]. The friction coefficient is assumed to be 0.15, and the boundary conditions utilized in the analysis are shown in Fig. 2. The residual stresses have limited influence on the load capacities of the tubular columns [3,9] and therefore the residual stresses were not considered in the present study.

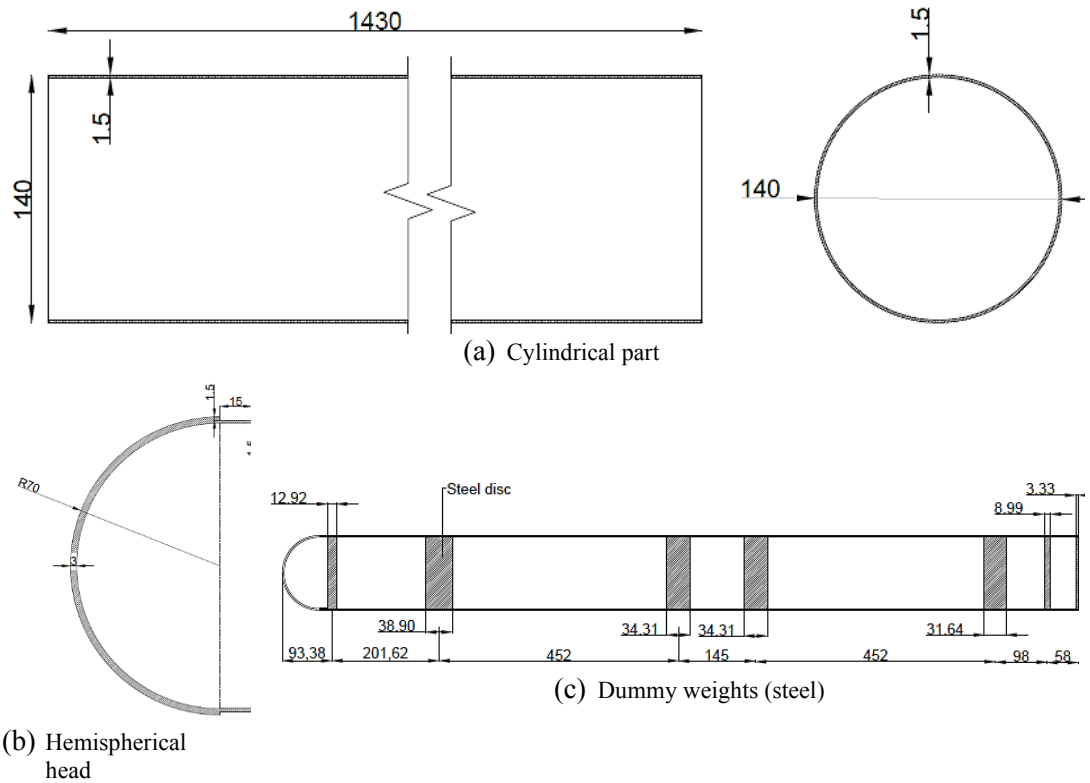

Figure 1. Details of the AA 2014-T6 projectile

Table 2. Johnson-Cook parameters for AA 2014-T6 and YSt310

Material	A	B	n	C
AA2014-T6	423.33	129.71	0.2677	0.0054
Steel (YSt 310)	460.00	334.55	0.4617	0.0130

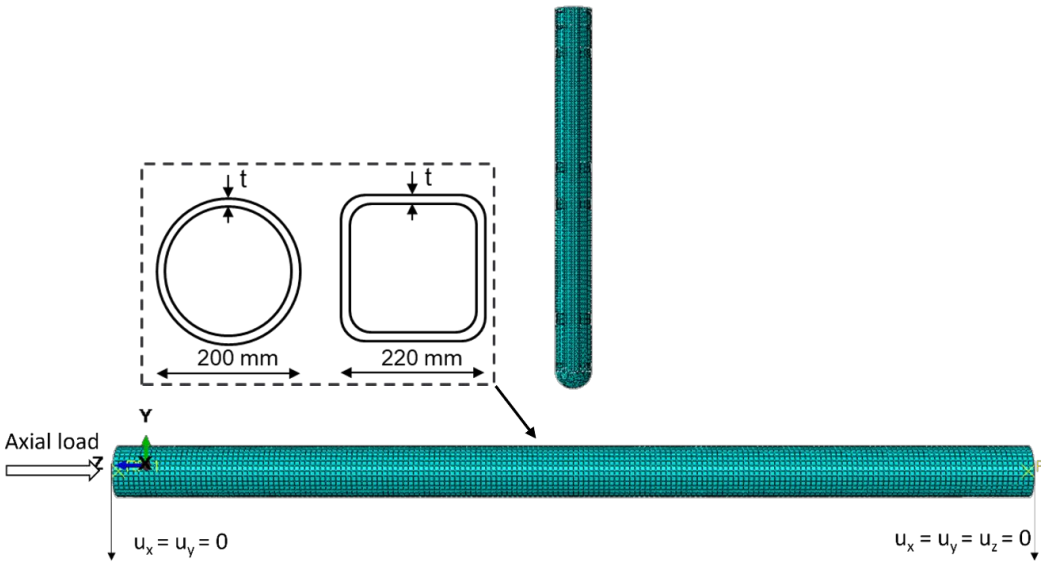

Figure 2. FE model with boundary conditions.

PARAMETRIC STUDIES

Table 3 outlines the framework for the numerical parametric investigation conducted in this study. The parameters studied were the diameter to thickness or side to thickness (*D/t*) ratio, axial load level (*n*), and impact direction. Axial load level (*n*) denotes the ratio of the applied axial load to the maximum axial capacity of the column. Each numerical model is designated with a unique specimen ID. For example, C-5-20 represents a circular specimen with a 5mm tube thickness and a 20% axial load level, while S-6-0 represents a square column with a 6mm tube thickness and 0% axial load level. SC-5-0 denotes a square column subjected to corner impact. The tube thickness for square and circular columns was varied as 5mm, 6mm, 8mm, and 10mm for the parametric analysis. The axial load level (*n*) was varied from 0%, 20%, 40% and 60% for the circular specimen. The impact velocity of 20 m/s was kept constant in all the analysis. In all the simulations, the direction of impact was perpendicular to the specimen and at the mid span. Only in the case of SC-5-0, the impact was at the corner of the square tube.

In instances where the specimen experiences axial loading, the analysis adopts a two-step procedure. Initially, an axial load is imposed via an axial force boundary condition. Subsequently, an impact velocity of 20 m/s is defined as the initial condition.

Table 3. Details of parametric study

Spec.ID	D/t	Load level (n)	Max. Impact force (kN)	Maximum local deformation (mm) in	
				Column	Projectile
C-5-0	40.00	0	230	49.58	24.56
C-5-20	40.00	0.2	223	53.5	22.5
C-5-40	40.00	0.4	218	59.21	19.37
C-5-60	40.00	0.6	214	66.59	16.59
C-6-0	33.33	0	314	19.74	42.93
C-8-0	25.00	0	380	14.15	47.24
C-10-0	20.00	0	387	11.33	49.75
S-5-0	44.00	0	340	47.16	14.93
S-6-0	36.67	0	421	36.49	24.27
S-8-0	27.50	0	496	23.36	36.55
S-10-0	22.00	0	496	11.22	48.68
SC-5-0	44.00	0	280	2.71	42.25

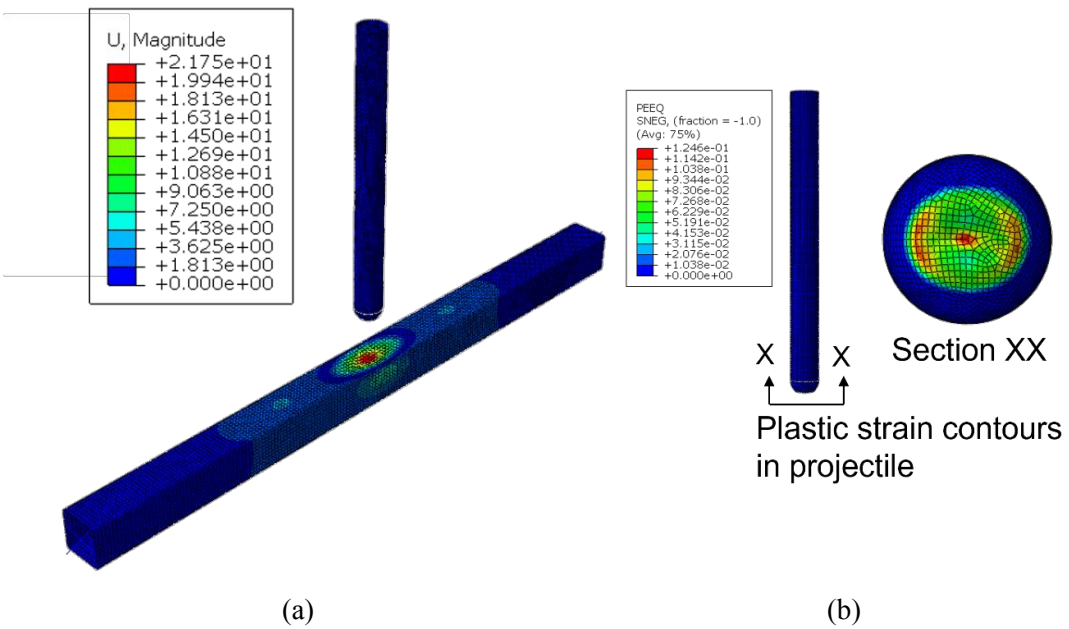

Figure 3. (a) Deformed shape of the projectile and S-10-0 column, (b) Plastic strain contours in projectile after impact

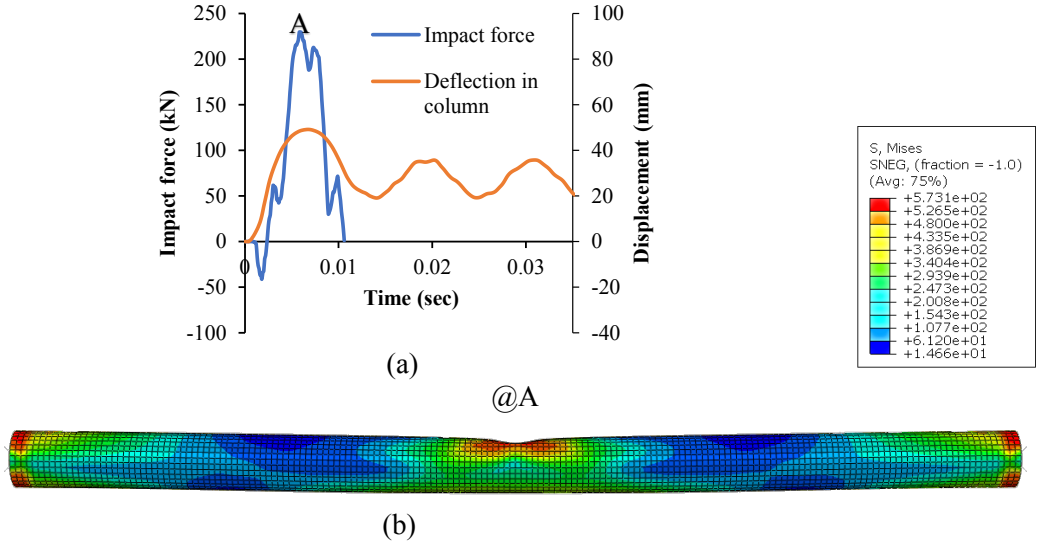

Figure 4. (a) Load and deformation time histories and (b) stress distribution at maximum impact force for C-5-0

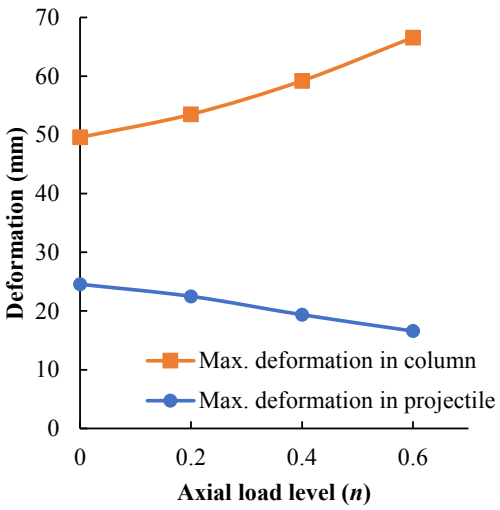

(a) Deformation vs axial load level in circular column

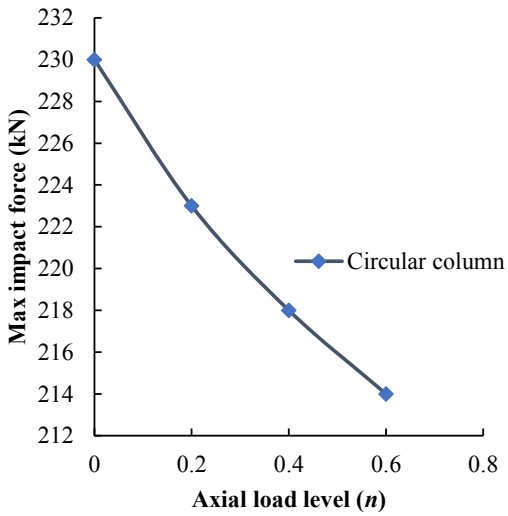

(b) Influence of axial load level on maximum impact force

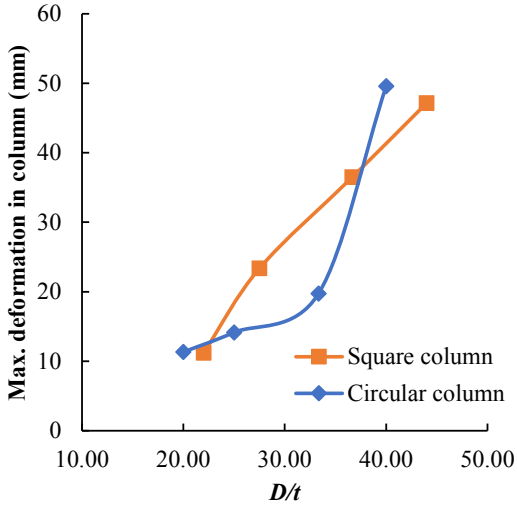

(c) Influence of D/t on maximum deformation in column

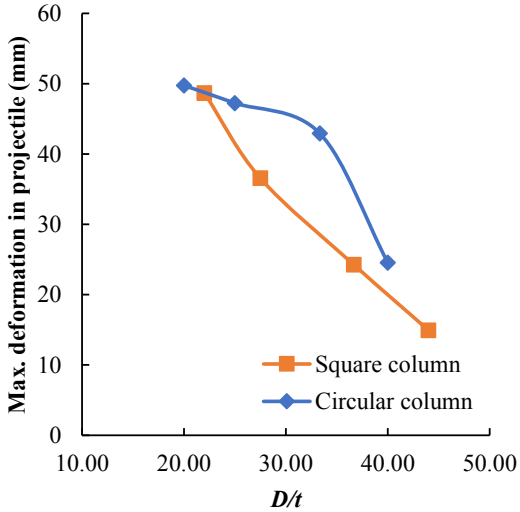

(d) Influence of D/t on maximum deformation in projectile

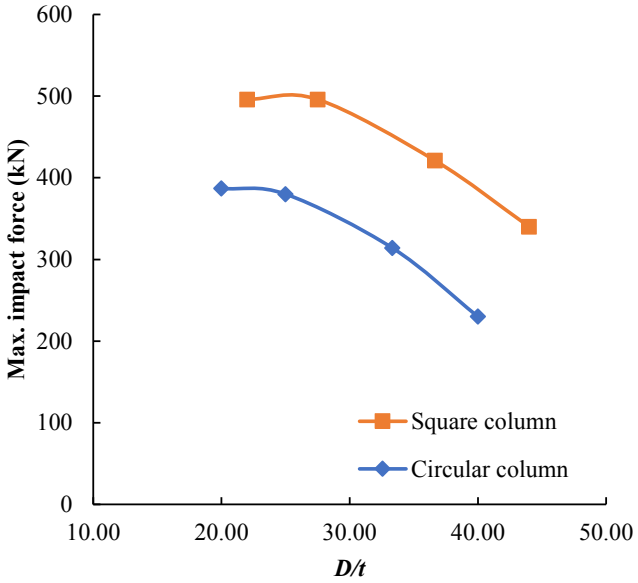

(e) Influence of D/t on maximum impact force

Figure 5. Influence of various parameters.

PARAMETRIC STUDY RESULTS

The simulation conducted in this study examined the impact of varying axial load levels (0%, 20%, 40%, and 60%) and *D/t* ratios of 40, 33.33, 25, and 20 for circular columns and 44, 36.67, 27.5, and 22 for square columns on the behavior of columns under impact. Fig. 3(a and b) shows the deformed shapes of the projectile and S-10-0 column. It can be observed from Fig. 3 that the damage was localized in the projectile across all scenarios, with deformation observed in the projectile head but no plastic strains noted in the cylindrical tube. From the FE simulations, the time history of impact force and deformation of column for C-5-0 is shown in

Fig. 4. In addition to the time histories, the failure shape with von-Mises stress distribution at maximum impact force (point A) is also shown in the Fig. 4. Fig. 5(a and b) illustrates that increasing axial load levels lead to a decrease in column impact resistance, accompanied by increased column deformation and decreased projectile deformation. The column subjected to a 60% axial load experienced a 34.31% increase in deformation compared to the no axial load condition. This phenomenon can be attributed to early yielding in columns with higher axial loads, resulting in reduced stiffness.

Regarding *D/t* ratios, Fig. 5(c and d) demonstrates that higher ratios correspond to increased maximum column deformation and decreased projectile deformation. Circular columns exhibited lower deformations compared to square columns for the same *D/t* ratio, attributed to additional stiffness from the arching action inherent in circular shapes. Increasing the *D/t* ratio reduced lateral and overall column stiffness, consequently decreasing impact resistance and increasing deformation. Fig. 5(e) shows that the maximum impact forces decrease as the *D/t* ratio increases for both circular and square columns.

In square columns, corner impacts showed greater stiffness in the plane perpendicular to the impact direction, leading to significantly less column deformation compared to side impacts. However, corner impacts resulted in higher projectile deformation.

CONCLUSIONS

Based on the parametric studies conducted, the following conclusions can be drawn:

1. Localized damage in the projectile suggests the potential for substituting materials in the cylindrical part for low-velocity impacts while keeping the total mass of the projectile constant.
2. Increasing column thickness reduces column deformation and increases impact resistance, and this can be attributed to the increase in stiffness with an increase in thickness.
3. Higher axial load levels lead to increased column deformation and decreased impact resistance.
4. Deformation in the projectile decreases when the thickness of the column decreases and when the axial load level increases.

REFERENCES

[1] Davis, JR. (1985) *Aluminium and Aluminum Alloys*. ASM Int, 42:746–9.
[2] Wardenier, J. (2011) *Hollow Sections in Structural Applications*. Geneva: 2nd Edition, CIDECT.
[3] Sangani, P., & Agarwal A. (2024). A comprehensive methodology for residual capacity evaluation of damaged steel tubular columns. *Journal of Construction Steel Research*, 216, 108625.
[4] Kueh ,ABH., Abo Sabah, SH., Qader, DN., Drahman, SH., & Amran, M. (2023). Single and repetitive low-velocity impact responses of sandwich composite structures with different skin and core considerations: A review. *Case Studies in Construction Materials* 18, e01908.

[5] Grytten, F., Børvik, T., Hopperstad, OS., & Langseth, M. (2009). Low velocity perforation of AA5083-H116 aluminium plates. *International Journal of Impact Engineering*, 36, 597–610.

[6] Li, W., Gu, YZ., Han, LH., Zhao, XL., Wang, R., Nassirnia, M., & Heidarpour, A. (2019). Behaviour of ultra-high strength steel hollow tubes subjected to low velocity lateral impact: Experiment and finite element analysis. *Thin-Walled Structures*, 134, 524–536.

[7] *ABAQUS/Standard User's Manual Volumes I-III and ABAQUS CAE Manual*.(2016), Dassault Systems Simulia Corporation, 226–230.

[8] Sangani, P., Kumar, D., Khaderi, S.N., Ghoshal, K., Agarwal, A. (2024). Numerical Analysis of Low-Velocity Deformable Projectile Impact on Steel Columns. In: Goel, M.D., Kumar, R., Gadve, S.S. (eds) Recent Developments in Structural Engineering, Volume 1. SEC 2023. Lecture Notes in Civil Engineering, vol 52. Springer, Singapore. https://doi.org/10.1007/978-981-99-9625-4_57.

[9] Zhu, JY., Chan, TM., & Young, B. (2019). Cross-sectional capacity of octagonal tubular steel stub columns under uniaxial compression. *Engineering Structures*, 184 , 480–494.

EFFECTS OF CONCRETE SPALLING ON THERMAL-INDUCED COMPRESSION FORCE IN RESTRAINED REINFORCED CONCRETE COLUMNS EXPOSED TO NON-STANDARD FIRE

Truong-Thang Nguyen[1], Tuan-Trung Nguyen[2], Thi-Nguyet-Hang Nguyen[3], Viet-Hung Dang[4], Tuan-Ninh Nguyen[5] and Ngoc-Phuong Nguyen[6]

[1] PhD, Hanoi University of Civil Engineering (HUCE), Vietnam, thangnt2@huce.edu.vn.

[2] PhD, Hanoi University of Civil Engineering (HUCE), Vietnam, trungnt2@huce.edu.vn.

[3] PhD, Hanoi University of Civil Engineering (HUCE), Vietnam, hangntn@huce.edu.vn.

[4] PhD, Hanoi University of Civil Engineering (HUCE), Vietnam, hungdv@huce.edu.vn.

[5] PhD Student, Hanoi University of Civil Engineering (HUCE), Vietnam, tuanninh1509@gmail.com.

[6] PhD, Hanoi Architectural University (HAU), Vietnam, phuong151@gmail.com.

Corresponding Author: Truong-Thang Nguyen, PhD, ACPE.

No.55 Giai Phong Rd., Hai Ba Trung Dist., Hanoi, Vietnam

Email: thangnt2@huce.edu.vn

ABSTRACT

When fire incidents occur in concrete frame buildings, a locally-heated column will be simultaneously subjected to non-standard fire attack, restraint, eccentric loads and concrete spalling. Coupled with the deteriorations of material strength and stiffness at elevated temperatures, concrete spalling may cause premature failure of the column. In this paper, the practical range of restraint due to the heated column's different thermal response against its adjacent framing structural elements, is studied numerically to compare with the result of a previously-published analytical approach. Then, experimental observations on concrete spalling of twelve full-scale reinforced concrete column specimens in three series cast from different concrete compressive strengths and subjected to simultaneous actions of uniaxial/biaxial bending, axial restraint, and non-standard fire exposure are presented. It was shown that the concrete spalling occurred earlier and more severely on the columns cast from higher concrete strength. Besides, biaxially-loaded columns were more susceptible to concrete spalling than those under uniaxial bending. Furthermore, the fire durations of the tested columns predicted by the finite-element model ignoring concrete spalling were all longer than those recorded experimentally. Finally, the authors introduce a Gaussian Process regression model that is capable of predicting the similar trends observed from both numerical and experimental studies.

Keywords: *Reinforced Concrete, Column, Structure, Fire, Spalling, Restrain.*

INTRODUCTION

When a local fire occur near to an individual column in a reinforced concrete (RC) frame structure, the member's free thermal elongation is constrained by surrounding structural members such as beams and other columns having different thermal responses, generating additional compression force within the locally-heated column, so-called thermal-induced compression force (T-iCF). This may result in a significant increase in the member's internal forces including compression force and bending moments and thus, coupled with deteriorations of materials' strength and stiffness in fire, may lead to a dramatic decrease of the column fire resistance [1-2]. Therefore, an accurate prediction of the restraint force development is of importance in the fire-resistant analysis of RC columns subjected to such an unfavourable fire condition.

So far, there have been a pronounced number of research works on RC columns subjected to simultaneous actions of axially- or eccentrically-loading, restraint and fire [1-30], including a series of studies conducted by the authors [13-17]. The axial restraint exerted onto locally-heated RC columns in fire was studied in prototype RC framed structures, and simplified equations were derived for columns located at interior, exterior, and corner positions on the layout [17]. A number of worked examples were carried and a practical range from 0.01 to 0.165 was determined for the restraint ratio [13,17]. This set the basis for the restraint ratios used in a fire test programme on three series of twelve full-scale RC columns. They were tested with different levels of initial axial load, axial restraint stiffness and uniaxial/biaxial eccentricities under a non-standard fire condition [13-15]. Then, an analytical model was proposed by the authors which is capable of taking into account all the effects of axial restraint ratio, eccentricity, initial load level, concrete strength, as well as uniaxial and biaxial bending on the development of T-iCF [13,16]. It was shown that the analytical and numerical analyses neglecting concrete spalling effect observed in the tests may not be capable of reflecting closely the development of restraint forces induced in columns. Hence, in this paper, the issue will be investigated in three steps. Firstly, the practical range of restraint ratio will be studied numerically to compare with the result of the previously-published analytical approach. Then, experimental observations on concrete spalling in the fire tests will be presented. Finally, a Gaussian Process regression model that is capable of predicting the similar trends observed from both numerical and experimental studies will be introduced.

NUMERICAL STUDY ON RESTRAINT RATIO

Figure 1(a) shows the layout of a typical storey (j) in a prototype RC framed building with the supporting columns at interior, exterior and corner positions, namely, $C^i(j)$, $C^e(j)$, and $C^c(j)$, respectively. The adjacent beams $B_x(j)$ and $B_y(j)$ framing to the columns have equal spans of L_x and L_y along x- and y-directions, respectively. Figures 1(b,c,d) are the perspective views when the aforementioned columns are respectively subjected to local heating in individual fire scenarios. It can be seen that the heated column tends to thermally expand in the vertical direction and exerts vertical forces onto the ends of all the beams framing into its lower and upper ends. Since the columns at the far ends of the adjacent beams are still unheated, the beams will undergo differential vertical movements of their ends and exert a vertical restraint

force through their own flexural stiffness back onto the heated column, leading to thermal-induced axial restraint to the column, which can be presented by a stiffness K_r. With the column axial stiffness of K_c, the ratio $\alpha_r=K_r/K_c$ is defined as the axial restraint ratio. It was determined by analytical derivations adopting simplified assumptions in [13,17] that the value of this restraint ratio α_r for RC columns is in a practical range of 0.01 to 0.148. In this section, this ratio will be investigated by numerical approach and compared to that obtained from the worked examples conducted by the authors in [17].

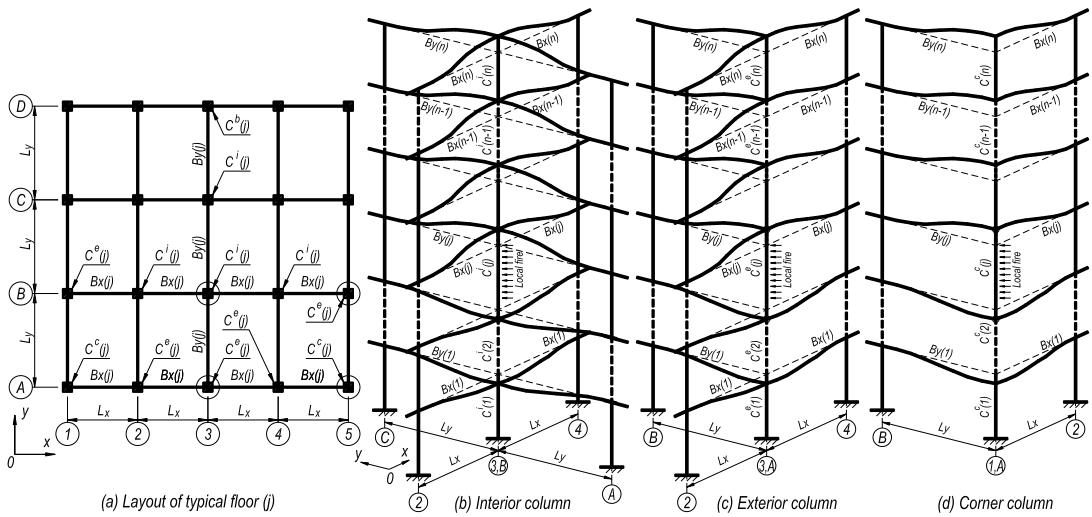

Figure 1. Scenarios of local fire on columns at different positions in prototype RC building.

In worked example No.1 of [17], RC buildings having typical layout shown in Figure 1 is studied. The beam spans in both directions are equal $L_x=L_y=L=6.0$ m. The cross-sections of typical beams and columns are 300×500 and 300×300 (in mm), respectively. The typical storey height is $H=3.3$ m. The number of storeys are varied from $n=1$ to the maximum value of $n=40$.

The frame structure is modelled and programmed using finite element software CSI ETABS as shown in Figure 2.

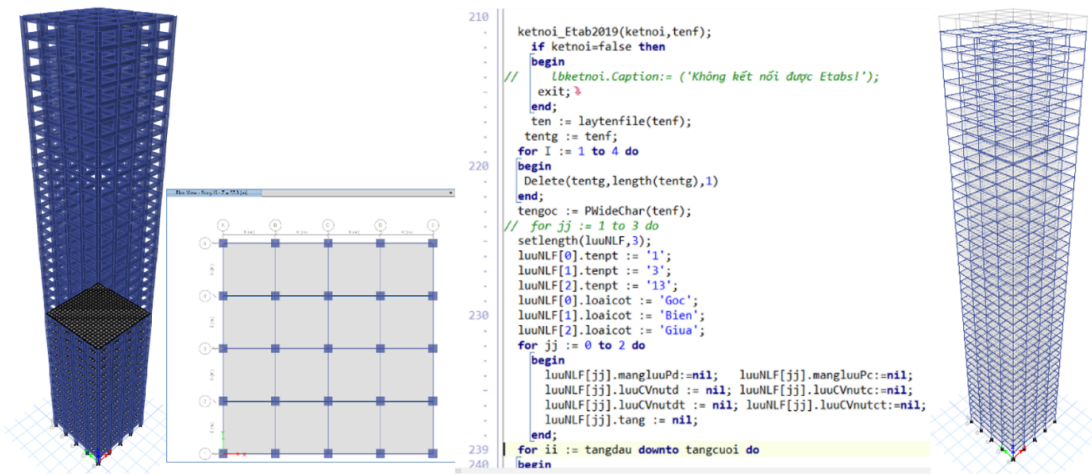

Figure 2. Modelling of worked example No.1 of [17] using CSI ETABS.

In order to automatically analyse the 40 numerical models having building heights varies from 1 to 40 storeys, the following steps are performed (Figure 2):

Step 1: Modelling the initial structure of a 40-storey building in ETABS. Connecting the software with CSI open-source Application Programming Interface (API) associated with coding language Embarcadero Delphi. It should be noted that the API is defined in the form of a .NET 4.7.1 dynamic link library and is implemented by ETABS. Besides, the structural analysis software must be installed both on the API client development machine, and on the client end-user's machine.

Step 2: Filtering all frame elements to determine columns at interior, exterior and corner positions for individual fire scenarios.

Step 3: Automatically assigning thermal load pattern to the locally-heated column.

Step 4: Automatically analysing the structure and exporting results of axial force and relative axial displacement of the investigated column, which can be used to determined the axial restrain stiffness K_r.

Step 5: Removing all structural elements in the top floor to obtain the next model, then return to Step 2 and repeat the loop until the 40th model which has only single storey.

The results obtained from numerical analysis are shown in Figure 3(b) and compared to those of analytical study in [17] shown in Figure 3(a).

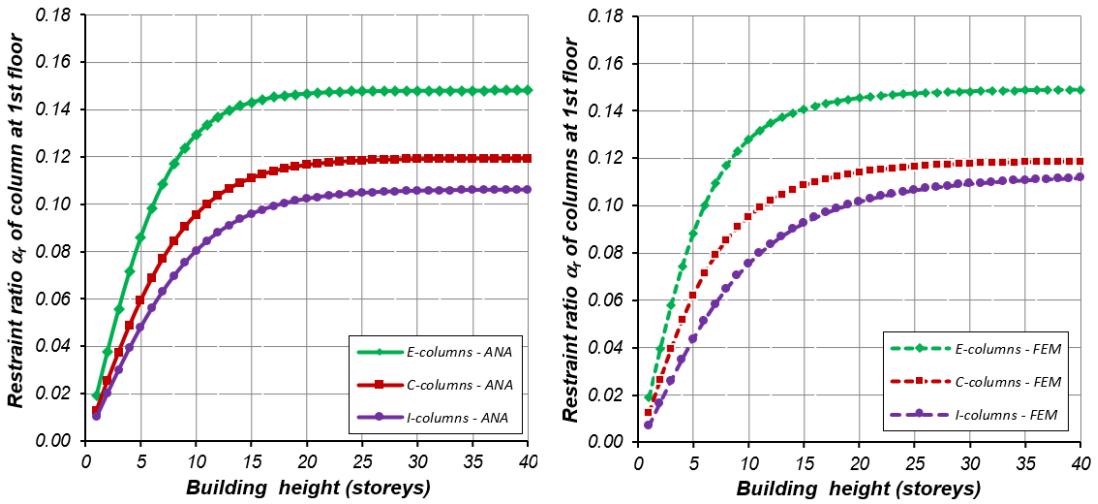

(a) Analytic results (b) Numerical results using CSI ETABS

Figure 3. Comparison results of worked example No.1 of [17].

Figure 3 shows that there are good agreements between numerical and analytical results in both the values and the trends of the curves. It is noted that with the exterior and corner columns of which the cracked cross-section were considered in [13,17], the effect of concrete spalling is also taken into account by using a similar reduction factor of the column in ETABS.

Similarly, the analytical and numerical analysis results of worked example No.4 of [17] are shown in Figure 4.

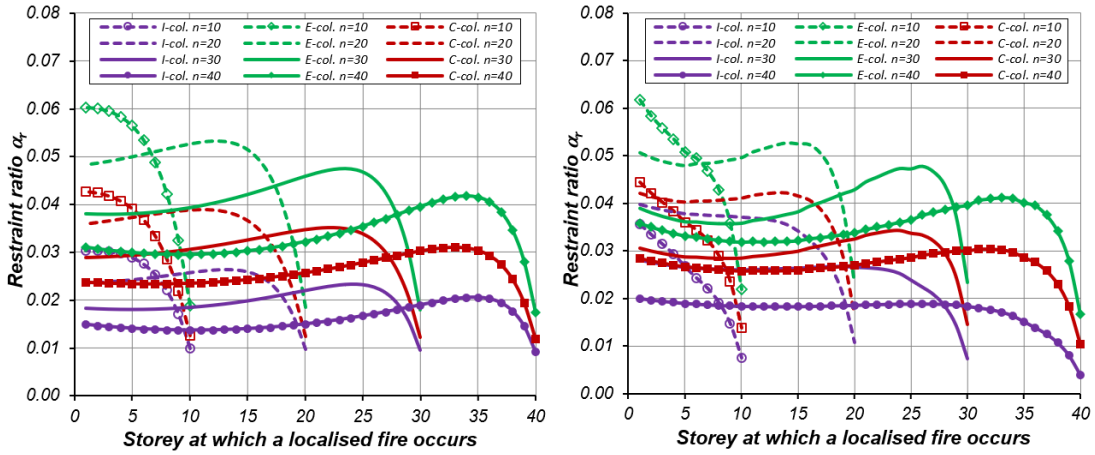

(a) Analytic results (b) Numerical results using CSI ETABS

Figure 4. Comparison results of worked example No.4 of [17].

The relatively good agreements in trend shown in Figures 3 and 4 also set a proper basis for the practical range of restraint ratio α_r to be used in the tests presented in the next section.

EXPERIMENTAL OBSERVATION ON CONCRETE SPALLING

Test specimens

This section reviews the observations of concrete spalling occurred on uniaxially- and biaxially-loaded RC column specimens subjected to axial restraint and non-standard fire exposure introduced by the author [14,15]. The experimental variables were uniaxial and biaxial eccentricities, restraint ratio, initial load level, and concrete compressive strength. Three test series including a total of twelve column specimens were proposed, as listed in Table 1.

Six test specimens in S1 series were subjected to different levels of uniaxial bending and initial applied load under restraint at elevated temperatures. Specimens C1-1-00 and C1-2-00 were loaded axially whereas the remaining four specimens, namely, C1-3-25, C1-4-40, C1-5-60 and C1-6-80, were loaded with uniaxial eccentricities of 25, 40, 60, and 80mm, respectively. Apart from an initial load level μ_{fi} of 0.45 applied for C1-1-00, this load factor was kept unchanged as 0.55 for C1-2-00 to C1-6-80. Fire tests were conducted on biaxially-loaded S2 specimens, namely, C2-1-25, C2-2-40, and C2-3-60, with similar levels of eccentricity, restraint ratio, and concrete strength with the respective specimens C1-3-25, C1-4-40, C1-5-60 of S1 series. Three column specimens in S3 series, namely, C1-3-25, C2-3-40, and C3-3-60, were tested under similar levels of biaxial eccentricity with S2 series. However, the differences between S2 and S3 specimens were (i) the mean concrete cylinder compressive strength of S2 was 55.3 MPa and that of S3 was 29.3 MPa; and (ii) the respective restraint ratio of S2 and S3 were 3.5% and 6.0%, which were all within the practical range determined in the previous section. This was to investigate the effects of restraint ratio and concrete strength on the structural behaviour of the test columns. It is noteworthy that the initial loads used in these fire tests were based on the eccentricity-dependent axial resistances of the test columns determined in accordance with design equations specified in EC2 Pt.1.1 [31]. The reduction factors μ_{fi} were also within an allowable range of 0.2 to 0.7 according to EC2 Pt.1.2 [32].

Table 1. Details of column specimens

Series	Specimens	Eccentricities (mm)		Restraint ratio α_r	Load level	Concrete strength	Rebar strength
		e_y	e_z	(%)	$\mu_{fi}=N_0/N_{Rd}^{EC2}$	(MPa)	(MPa)
S1	C1-1-00	0	0	3.6	0.45	55.3	550.2
	C1-2-00	0	0		0.55		
	C1-3-25	0	25		0.55		
	C1-4-40	0	40		0.55		
	C1-5-60	0	60		0.55		
	C1-6-80	0	80		0.55		
S2	C2-1-25	25	25	3.5	0.55	55.3	550.2
	C2-2-40	40	40		0.55		
	C2-3-60	60	60		0.55		
S3	C3-1-25	25	25	6.0	0.55	29.3	553.5
	C3-2-40	40	40		0.55		
	C3-3-60	60	60		0.55		

All the full-scale column specimens had identical geometric properties of 300 mm square cross-section and 3.3 m height. S1 and S2 specimens, which were cast in the same batch, had concrete with f_c=55.3 MPa and reinforcement of 6T20 and R8@250 with corresponding mean yield strengths of 550 and 496 MPa, respectively. For S3 specimens, the concrete cylinder strength was f_c=29.3 MPa; main reinforcing bars were 4T25 with f_y=553.5 MPa; and stirrups were R8@250 with f_y=496 MPa. Cement type I, siliceous aggregates with the maximum size of 20 mm, and concrete slump of 70 mm were specified for all test specimens.

Other details and instrumentations of the column specimens, as well as of the test schedule can be referred to in the published articles of the authors [14-16].

Test results

In S1 series, it was observed from testing that concrete spalling occurred in specimens C1-1-00 to C1-5-60. Due to the wrapping of steel meshes around the specimens to protect the furnace heating elements from concrete debris, it was impossible to capture concrete spalling images within the enclosed furnace. Hence, concrete spalling could only be recorded when there was either a gentle or an explosive sound heard from the furnace. The times at which concrete spalling were recorded in the C1-1-00 test are shown in Figure 5. It is shown that the first gentle noise was recorded at 161 min, followed by other noises of cracking and spalling at 216, 243, 269 and 288 min. Temperature of concrete surface when the first concrete spalling occurred was 328°C. The column failed at 310 min with a loud noise of explosive spalling. For C1-2-00, C1-3-25, C1-4-40 and C1-6-80, the first concrete spalling was recorded at 149, 154, 167, and 160 min, with the corresponding surface temperatures of 276, 297, 354, and 320°C,

respectively. In the C1-5-60 test, a loud noise of explosive spalling was recorded at 159 min followed by premature failure.

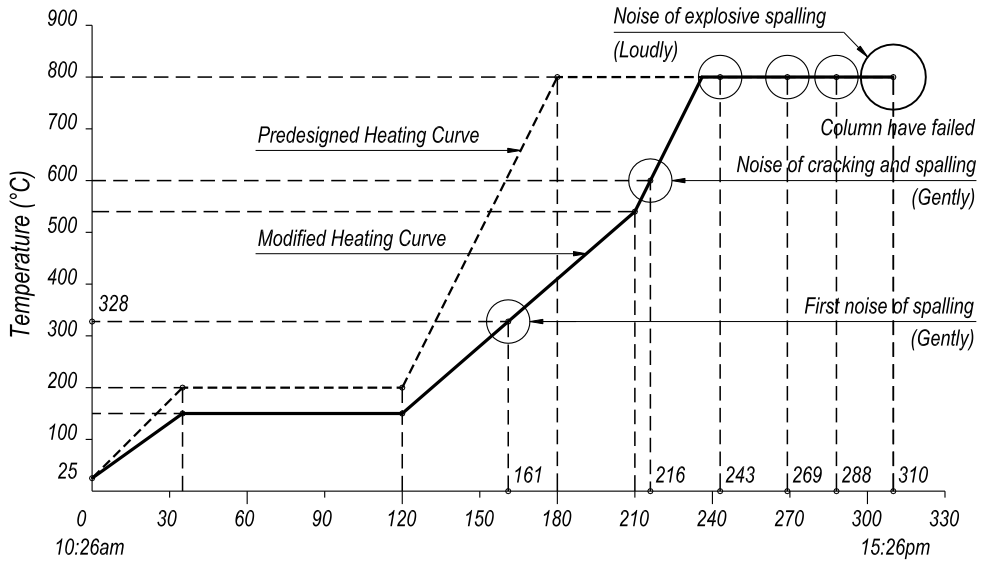

Figure 5. Time and temperature of concrete spalling of column specimen C1-1-00 [14].

The first concrete spalling times and the corresponding temperatures recorder in all the specimens are listed in Table 2.

Table 2. First concrete spalling time and corresponding temperatures

Series	Specimens	Time (min)	Temperature (°C)	Average temperature (°C)
S1	C1-1-00	161	328	318
	C1-2-00	149	276	
	C1-3-25	154	297	
	C1-4-40	167	354	
	C1-5-60	159	319	
	C1-6-80	-	-	
S2	C2-1-25	160	323	312
	C2-2-40	160	323	
	C2-3-60	152	286	
S3	C3-1-25	178	401	393
	C3-2-40	173	380	
	C3-3-60	177	397	

It is shown in Table 2 that for S1 series, the average spalling temperature was 315ºC. For S2 and S3 series, concrete spalling started to occur at 152 to 160 min and 173 to 178 min, with the corresponding average surface temperatures of 312 and 393ºC for S2 and S3 specimens, which had concrete cylinder strength of 55.3 and 29.3 MPa, respectively. This clearly illustrates that columns cast from a higher concrete strength were more susceptible to concrete spalling.

Images of spalled concrete debris captured after testing are shown in Figure 6, in which the outermost concrete cover spalled off from the column cross-section.

Figure 6. Debris of spalled concrete from tested specimens

Figure 6 shows that for S2 specimens with a higher concrete strength of 55.3 MPa, concrete spalling occurred at the corners of cross-section with a typical length of about 250 mm and a typical width varying from 40 to 60 mm. For S3 specimens which had a lower concrete strength of 29.3 MPa, concrete spalling mainly occurred at the column surfaces away from the corners at smaller chunks with typical dimensions of 150 to 250 mm and a typical thickness of 20 to 30 mm (Figure 6). The image of the typical failed specimen C1-1-00 is shown in Figure 7.

Figure 7. Spalling Image of column specimen C1-1-00 after test

When the column specimens were exposed to non-standard fire during tests, high thermal gradients caused the surface layers to expand and eventually crack or spall off. As a result, the cooler, interior parts of the concrete and the reinforcing steel were exposed to fire attack and hence, another process of heat transfer was generated. It was also observed from the tests that the durations from the start of the experiment to the failure of all the specimens, so-called fire duration, were adversely affected by cracking and spalling. These phenomena not only changed the heat transfer process but also reduced the bond between concrete and reinforcing bars, leading to a pronounced reduction in load-bearing capacity of the columns. Comparing test results between the couples C1-3-25 and C2-1-25, C1-4-40 and C2-2-40; C1-5-60 and C2-3-60, it was showed that the biaxially-loaded columns were more susceptible to concrete spalling than those under uniaxial bending.

ANALYTICAL MODEL FOR PREDICTION OF T-iCF

Analytical derivation of T-iCF

In the experimental programme introduced the previous section, the thermal-induced compression force (T-iCF) ΔN_a^T were also measured to investigate its relation with the restraint ratios applied [13-16]. Then, the development of the ratio between ΔN_a^T and the initial compression force N_0, so-called the normalised restraint forces, were also studied comprehensively using analytical approach [16]. The comparison results between the experimental and analytical approaches are recalled in Figure 8 [16], from which it can be seen that: (i) The development of normalised restraint forces increase with restrain ratio and load uniaxial eccentricity but decrease with initial load levels; (ii) Normalised restraint forces increase with biaxial eccentricity and restraint ratio; (iii) Normalised restraint forces are more susceptible to biaxial bending compared to uniaxial bending; and (iv) The numerical analyses which ignore concrete spalling tend to overestimate normalised restraint forces.

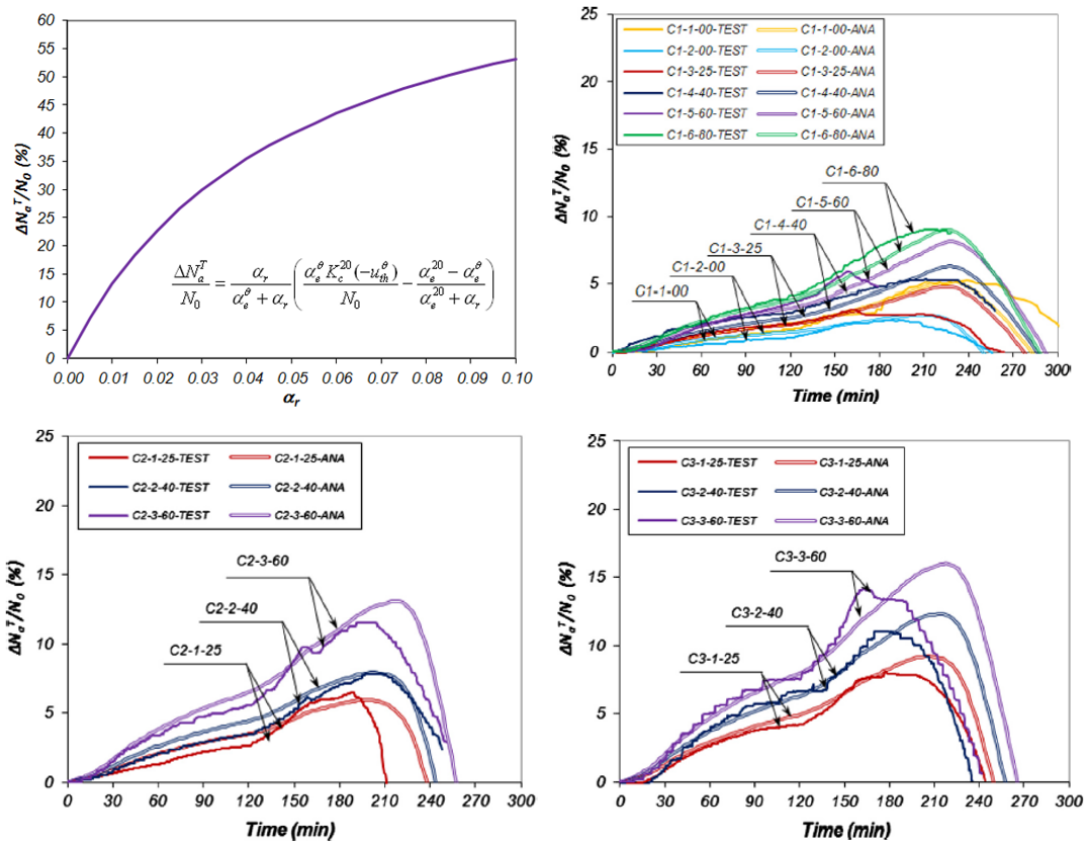

Figure 8. Comparison results of normalized restraint forces [16]

In the next section, a data-driven approach based on Gaussian Process (GP) regression will be presented for predicting the behaviour of restrained RC columns subjected to fire. It is noteworthy that the performance of GP objectively depends on the database under investigation rather than some subjective assumptions and takes into account the effect of concrete spalling observed in the fire test conducted.

Gaussian Process regression for T-iCF

In the data science field, there is a vast number of models for establishing a prediction model ranging from simple linear regression models to over-parameter deep learning with complex and very deep architecture such as Transformer. However, when working with experimental data obtained from real structures, most models encounter a persistent and challenging problem of limited data availability, characterized by small dataset sizes and few feature values. Hence, utilizing a model with many hyperparameters on small-size data will certainly lead to the overfitting problem, i.e., it can fit approximately perfectly on training data but provide non-physical, counter-intuitive results on unseen data. On the other hand, generating more reliable experimental data is very difficult because conducting experiments with real structures is expensive, tedious, and time-consuming. Therefore, in this study, the authors propose a parsimonious model based on Gaussian Process (GP) regression that has only a few parameters to determine but still appropriately fits the training data and provides admissible prediction results on new data.

The GP model has a simple yet effective intuition that the more input data samples are similar, the more corresponding outputs are correlated, and vice versa. In addition, the GP model is rigorously supported by the Bayesian theory regarding the conditional probability of prediction results on observed data, as demonstrated in [33]. The most critical component of GP is the kernel function, which measures the similarity between data samples. The kernel function is problem- and data-specific; there is no universal function that always yields highly accurate results for different databases of various dimensionality, ranges of values, and data sizes. Some popular kernels of GP are linear kernel, polynomial kernel, constant kernel, radial basis function (RBF), dot product kernel, etc [34]. Actually, the authors tried various types of kernel functions and found that no single kernel can provide satisfactory performance on new data despite good results on training data. Hence, the authors considered combining various kernels into one compound function to create a higher-performance model. A trial-and-error process was implemented to explore different combinations, including adding and multiplying kernels. Eventually, starting with the popular RBF kernel, then multiplying it with a constant kernel for improved scaling ability, and adding a polynomial kernel to capture the global trend of data, along with a white Kernel accounting for environmental noise, the proposed compound kernel is formulated in Eq. (1), provided that the final values of coefficients A_1, A_2, A_3 and A_4 are determined via the training process:

$$Kernel = ConstantKernel(A_1) * RBF(A_2) + ConstantKernel(A_3) * PairwiseKernel('poly', 'degree': 2) + WhiteKernel(A_4) \quad (1)$$

Data preparation

In terms of data preparation, the experimental data of columns C1-1-00, C1-2-00, C1-3-25, C1-4-40, C1-5-60, C1-6-80, C2-1-25, C2-2-40, C2-3-60, C3-1-25, C3-2-40, C3-3-60 presented in Figure 8 were utilized as training and validation datasets. More specifically, the input features include load eccentricities in y- and z-directions, concrete compressive strength, steel yield strength, rebar ratio, load level, restraint ratio, and time instant, whereas the output of interest is the ratio $\Delta N_a^T / N_0$. The experimental database was reorganized and presented under a tabular form, with 10 columns, including the index number, column name, seven input features, and

the output values as mentioned above. There are a total of 4543 rows of data, i.e., data samples. It is noted that the GP has only a small number of parameters to determine; thus, only a small fraction of data is required as training data. Hence, the database was randomly divided into two non-overlapping datasets, namely training and validation, with a ratio of 15:85. The training and validation datasets have around 681 and 3862 data samples, respectively.

Analysis results of Gaussian Process regression for T-iCF

After the data preparation step was accomplished, the Gaussian Process model with compound kernel function described in Eq.(1) is defined and trained with the help of the Python scikit-learn library, on an ordinary laptop equipped with Intel core i7-10750, 32 GB RAM. After that, the trained model is utilized to replot the evolution curves of $\Delta N_a^T/N_0$ for all 12 experimental columns as shown in Figure 9. It can be seen that by only utilizing 15% of the experimental data, the GP model with the proposed compound kernel can accurately replicate the complete evolution curves because the prediction curves closely align with the experimental curves.

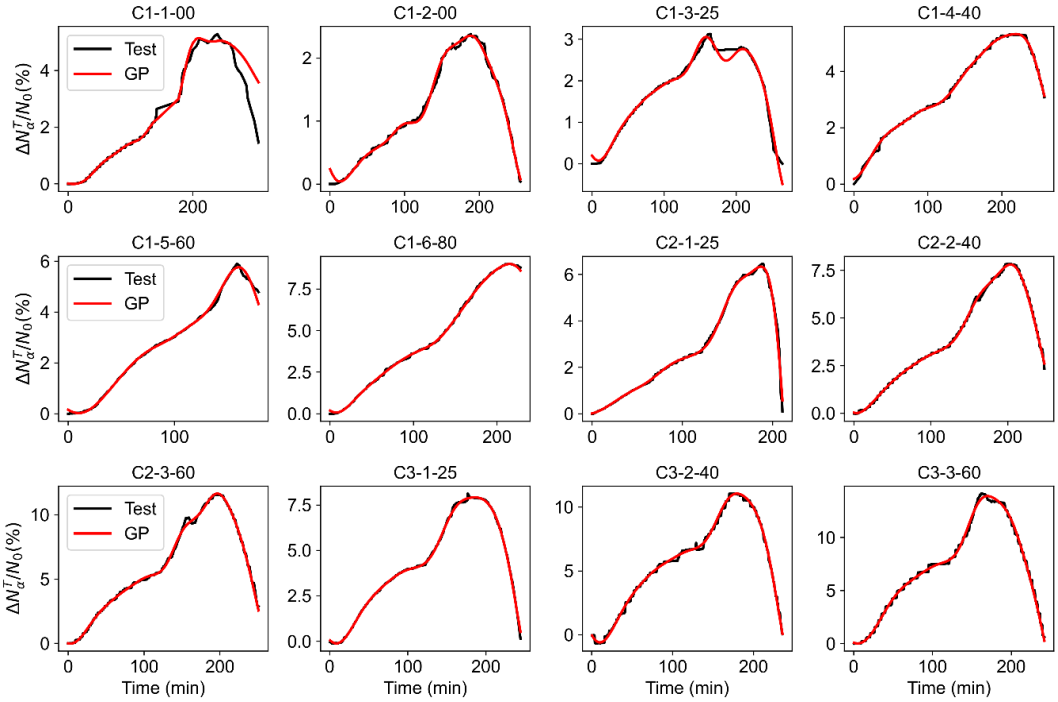

Figure 9. Comparison results of Gaussian Process model with experiments

More appealing, the GP model is employed to predict the behaviours of restrained columns with new input values, for example, uniaxial eccentricities of 20, 30, 50, 70 mm for columns C1, biaxial eccentricities of 30, 50, 55 mm for columns in S2 series, biaxial eccentricities of 35, 50 mm S3 series, and new concrete compressive strengths of 35, 45, 50 MPa for S3 series. These prediction results are demonstrated in Figure 10. Qualitatively and visually, these results follow the global trend of experimental data. They also respect the intuitive order of the effect of input parameters; for example, the $\Delta N_a^T/N_0$ curve with a higher value of concrete compressive strength will be positioned lower (Figure 10(d)), or a higher eccentricity value will result in a higher value of the ratio $\Delta N_a^T/N_0$. On the other hand, these curves obtained by

GP allow quantitatively estimating these intuitions. These predictions may not be perfectly exact, but they can reflect the effect of spalling on restrained RC columns under fire to some extent, which is still infeasible with analytical/numerical models.

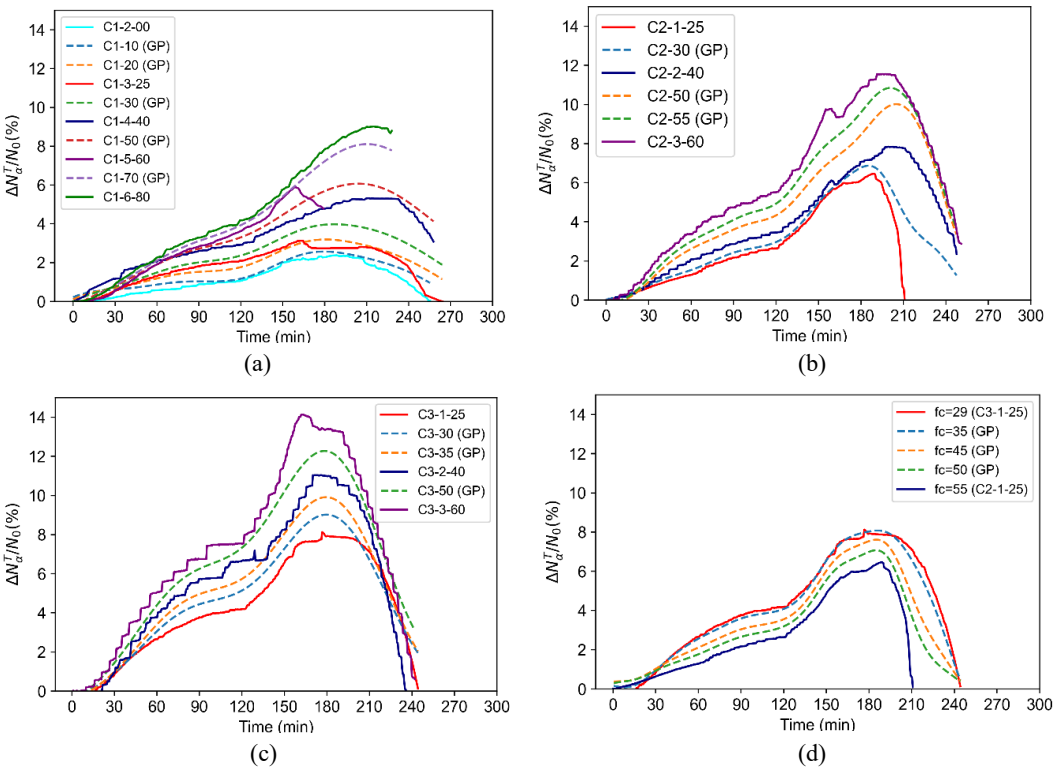

Figure 10. Prediction results by Gaussian Process for columns with new input data

CONCLUSIONS

In this article, the effect of concrete spalling on thermal-induced compression force in reinforced concrete columns exposed to non-standard fire exposure is investigated using three approaches. Firstly, the numerical analysis using CSI ETABS confirms the practical range of (0.01, 0.148) of the restraint ratio on a locally-heated RC columns in frame structures that was proposed by analytical method in another published research of the authors. Then, a fire test programme was conducted on twelve full-scale RC columns with the restraint ratios within the above range and loaded by uniaxial and biaxial bending. It was observed that the concrete spalling occurred earlier and more severely on the columns cast from higher concrete strength. Besides, biaxially-loaded columns were more susceptible to concrete spalling than those under uniaxial bending. Finally, a Gaussian Process regression model is introduced with data for training taken from fire tests. It is shown that the proposed model is capable of overcoming the shortcoming of analytical model ignoring concrete spalling and of predicting a closed trend for the negative effect of this disadvantage phenomenon on RC columns in fire. For the future works, the validation of the proposed model will be conducted in a more comprehensive manner with additional experimental and numerical data collected from literature.

ACKNOWLEDGMENTS

The authors would like to thank the Nanyang Technological University (NTU, Singapore) for providing financial support for the experimental study reviewed herein. Professor Tan Kang Hai's encouragement on the research idea is deem appreciated. The authors' thankfulness is also extended to the Hanoi University of Civil Engineering (HUCE, Vietnam) for providing supports in administration issues.

REFERENCES

[1] Lie, T.T., Line, T.D.. (1985). Influence of restraint of fire performance of reinforced concrete columns. *First international symposium, International Association for Fire Safety Science*.

[2] Wang, Y.C., Moore, D.B. (1994). Effect of thermal restraint on column behaviour in a frame. *The fourth International Symposium of Fire safety science*, Ottawa, 1055-1066.

[3] Ali, F., Nadjai, A., Silcock, G., Abu-Tair, A.. (2004). Outcomes of a major research on fire resistance of concrete columns. *Fire Safety Journal* 39, 433-445.

[4] Benmarce, A., Guenfoud, M.. (2005). Experimental behaviour of high-strength concrete columns in fire. *Magazine of Concrete Research* 57(5), 283-287.

[5] Tan, K.H., Toh, W.S., Phng, G.H., Huang, Z.F.. (2007). Structural responses of restrained steel columns at elevated temperatures. Part 1: Experiments. *Eng Struct* 29, 1641-1652.

[6] Huang, Z.F., Tan, K.H. (2007). Structural response of restrained steel columns at elevated temperatures. Part 2: FE simulation with focus on experimental secondary effects. *Eng Struct* 29, 2036-2047.

[7] Huang, Z.F., Tan, K.H., Phng, G.H. (2007). Axial restraint effects on the fire resistance of composite columns encasing I-section steel. *J Constr Steel Res* 63, 437-447.

[8] Kodur, V.K.R., Raut, N. (2008). Fire Resistance of Reinforced Concrete Columns - State-of-the-art and Research Need". *ACI Special Publication*, 255, 97-124.

[9] Wu, B., Li., Y-H. (2009). Experimental study on fire performance of axially-restrained NSC and HSC columns. *Structural Engineering and Mechanics* 35(5), 635-648.

[10] Kodur, V., Dwaikat, M., & Raut, N. (2009). Macroscopic FE model for tracing the fire response of reinforced concrete structures. *Engineering Structures*, *31*(10), 2368-2379.

[11] Martins, A.M.B., Rodrigues, J.P.C. (2010). Fire resistance of reinforced concrete columns with elastically restrained thermal elongation. *Engineering Structures* 32(10), 3330-3337.

[12] Raut, N., & Kodur, V. (2011). Response of Reinforced Concrete Columns under Fire-Induced Biaxial Bending. *ACI structural journal*, 108(5).

[13] Nguyen, T-T. (2013), *Structural behaviour and fire-resistant analysis of reinforced concrete columns at elevated temperatures*. PhD Thesis, Nanyang Technological University (NTU), Singapore.

[14] Tan, K.H., Nguyen, T-T. (2013). Structural responses of reinforced concrete columns subjected to uniaxial bending and restraint in fire. *Fire Safety Journal*, 60, 1-13,.

[15] Tan, K.H., Nguyen, T-T. (2013). Experimental behaviour of reinforced concrete columns subjected to biaxial bending and restraint at elevated temperatures. *Engineering Structures Journal*, 56, 823-836.

[16] Nguyen, T-T., Tan, K.H. (2014). Thermal-induced restraint forces of heated columns in concrete framed structures. *Fire Safety Journal*, 69, 136-146.

[17] Nguyen, T-T., Tan, K.H. (2014). Fire-induced restraint to columns in framed concrete buildings", *Proceedings of the Eighth International Conference Structures in Fire (SIF 2014)*, Shanghai. 319-326.

[18] Rodrigues, J. P. C., Laím, L. M., & Korzen, M. (2014). Fire behaviour of circular concrete columns with restrained thermal elongation. *Journal of advanced concrete technology*, *12*(9), 289-298.

[19] Bamonte, P., & Monte, F.L. (2015). Reinforced concrete columns exposed to standard fire: Comparison among different constitutive models for concrete at high temperature. *Fire Safety Journal*, *71*, 310-323.

[20] Albrifkani, S., & Wang, Y. C. (2016). Explicit modelling of large deflection behaviour of restrained reinforced concrete beams in fire. *Engineering Structures*, *121*, 97-119.

[21] Haksever, A. (2017). Experimental and Computational Investigation of Fire Behavior of Restrained Reinforced Concrete Columns-Part II. *Trakya Üniversitesi Mühendislik Bilimleri Dergisi*, *18*(2), 121-136.

[22] Kodur, V., Hibner, D., & Agrawal, A. (2017). Residual response of reinforced concrete columns exposed to design fires. *Procedia engineering*, *210*, 574-581.

[23] Liu, J. C., Tan, K. H., & Yao, Y. (2018). A new perspective on nature of fire-induced spalling in concrete. *Construction and Building Materials*, *184*, 581-590.

[24] Džolev, I., Cvetkovska, M., Lađinović, Đ., & Radonjanin, V. (2018). Numerical analysis on the behaviour of reinforced concrete frame structures in fire. *Comput. Concr*, *21*(6), 637-647.

[25] Gernay, T. (2019). Fire resistance and burnout resistance of reinforced concrete columns. *Fire safety journal*, *104*, 67-78.

[26] Buttignol, T. E. T., & Bittencourt, T. N. (2021). Simplified design procedures for the structural analysis of reinforced concrete columns in fire. *Engineering Structures*, *246*, 113076.

[27] Mahmoud, K. A. (2021). Lateral deformation behavior of eccentrically loaded slender RC columns with different levels of rotational end restraint at elevated temperatures. *Journal of Structural Fire Engineering*, *12*(1), 35-64.

[28] Ni, S., & Gernay, T. (2021). Considerations on computational modelling of concrete structures in fire. *Fire safety journal*, *120*, 103065.

[29] Mahmoud, K. A. (2022). Overview of factors affecting the behavior of reinforced concrete columns with imperfections at high temperature. *Fire Technology*, *58*(2), 851-887.

[30] Yao, Y., Zhang, H., Zhu, Y. F., & Liu, Y. (2023). Progressive collapse resistance of reinforced concrete beam-column connection under fire conditions. *Structures* (Vol. 47, pp. 1265-1283). Elsevier.

[31] EN 1992-1-1, *Eurocode 2. Design of Concrete Structures - Part 1-1: General Rules and Rules for Buildings* . CEN, 2004.

[32] EN 1992-1-2, *Eurocode 2. Design of Concrete Structures - Part 1-2: General Rules, Structural Fire Design*. CEN, 2004.

[33] Williams, C. K., & Rasmussen, C. E. (2006). *Gaussian processes for machine learning* (Vol. 2, No. 3, p. 4). Cambridge, MA: MIT press.

[34] Wilson, A., & Adams, R. (2013, May). Gaussian process kernels for pattern discovery and extrapolation. *International conference on machine learning* (pp. 1067-1075). PMLR.

PROTECT2024